Nanostructured Metamaterials for Thermal Applications

by

Huan Hu

A thesis submitted in partial fulfillment of the requirements for the degree of

Master of Science

in

Photonics and Plasmas

Department of Electrical and Computer Engineering
University of Alberta

Abstract

Metamaterials are artificially engineered materials with tailored properties for applications in imaging, sensing, waveguiding and quantum optics. Even though they hold the potential for transformative impact, industrial applications have been impeded by large absorption losses in material properties. This thesis puts forth thermal applications of metamaterials where optical losses are a necessary design component and can be fruitfully utilized for applications. A wide range of metamaterial designs have been numerically studied and optimized for applications as narrowband perfect absorbers/emitters in the near-infrared wavelength region compatible with low bandgap thermophotovoltaic cells.

We study the collective polaritons of nanowire and thin film metamaterials to show that their selective absorption and thermal emission properties could be used for thermophotovoltaic applications. The design and simulation results are in excellent agreement with initial the results of experiments on metallic nanowire arrays in a dielectric host matrix. We also evaluate the contribution of phonon-polaritons to thermal conductivity of silicon carbide nanowire arrays. The comprehensive analysis of collective metamaterial modes and analytical tools developed in the thesis can aid future design and optimization of thermal metamaterials.

I would like dedicate this work to my mother, Xiyu Wan, and my father, Pinghe Hu, for their tolerance, support and endless help

Acknowledgements

I have stayed in Edmonton for 2 years to finish my Master of Science program. It is not a long time in my study career as a student. But the memory will last a long time, because of the people who offered me selfless help and support, the people who guided me, and the people who worked together with me.

Foremost, I would like to express my sincere gratitude to my supervisor Dr. **Zubin Jacob** and Dr. **Sandipan Pramanik** for the continuous support of my M.Sc study and research. Especially Dr. Zubin Jacob who kept offering me valuable advice and meaningful discussions in research. He taught me how to do research correctly and as a result I learned a lot during the last 2 years. Actually, he is more than an academic supervisor because he truly cares about his students' future careers rather than only focusing on research progress. Finally, I would like to thank him for his tolerance and encouragement when I lacked motivation and got confused in my life.

I would also like to thank the helpful and talented students in my lab, i.e. **Cristian L. Cortes,Prashant Shekhar, Saman Jahani, Sean Molesky, Ward Newman, Yu Guo, Jonathan Atkinson and Farid Kalhor**. They are more friends than colleagues, making graduate life in Edmonton more wonderful.

At last, I would like to thank my parents for understanding and supporting my study abroad, bearing the pain of missing a child.

Contents

List of Figures

List of Tables

List of Abbreviations and Symbols

Abbreviation	Extended Form
EMT	Effective Medium Theory
PEC	Perfect Electric Conductor
TPV	Thermophotovoltaics
ENZ	Epsilon-Near-Zero
ENP	Epsilon-Near-Pole
HMM	Hyperbolic Metamaterial
DOS	Density of States
SPP	Surface Plasmon Polariton
NW	Nanowire
ML	Multilayer
λ	Wavelength

Chapter 1

Introduction

Metamaterials are artificial photonic media with electromagnetic properties unavailable in naturally occuring media. This field of research uses designer nanostructures embedded in host media for engineering dielectric constants (refractive index). Metamaterials can dramatically increase the functionality of conventional devices and have shown promise in sub-diffraction imaging [1, 2, 3, 4], sub-wavelength waveguiding [5], optical sensing [6] and invisibility [7].

1.1 Engineered Polaritons

The key concept that allows for optical engineering of materials is the presence of polaritons: these are collective light-matter excitations that have properties distinct from photonic modes. Polaritonic media are the building blocks of metamaterials.

1.1.1 Plasmon-Polaritons

In the case of metals, the sea of free electrons can have a collective oscillation known as the bulk plasmon (Fig. 1.1(a)). This occurs at the characteristic plasma frequency (ω_p) of the metal which is close to the ultraviolet spectral range for most metals like silver and gold. An interesting situation occurs in the case of thin films or nanorods of plasmonic metals (Ag, Au). These free electrons can strongly couple to free space radiation leading to a surface plasmon-polariton [8] which have high field concentrations in nanoscale volumes of the thin films or nanorods. Such field enhancement and strong confinement of light cannot occur for simple dielectric media such as glass nanorods.

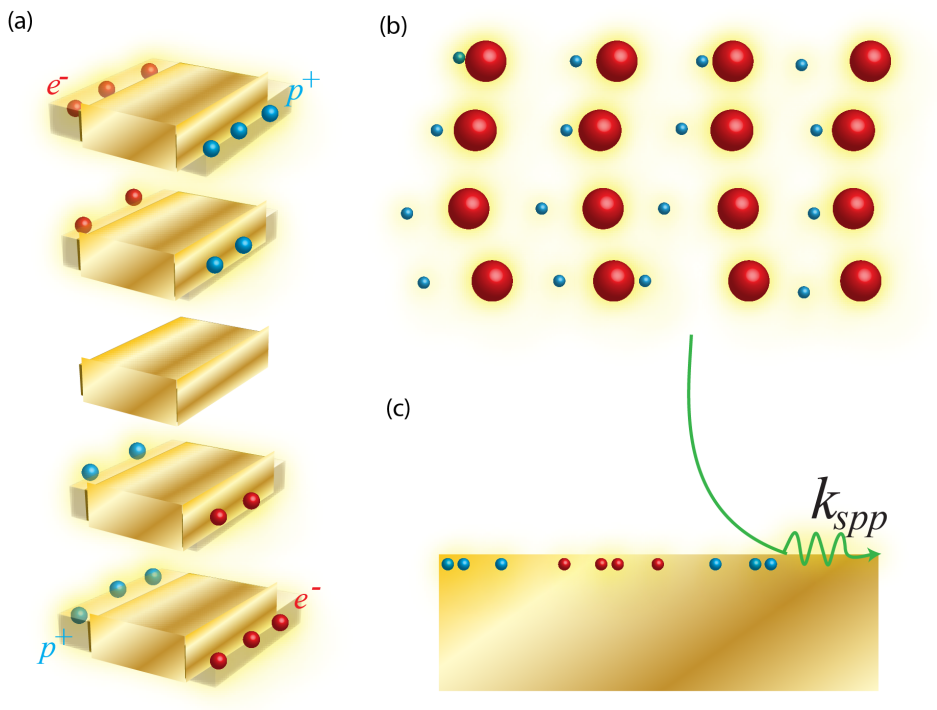

Figure 1.1: Schematics of plasmons and phonons. (a) Bulk plasmons (which comes from the collective oscillation of free electrons in the metal eg. silver, gold, etc). (b) Optical phonons in a diatomic system (eg. sodium chloride ionic crystal). The movement of atoms in an optical vibration mode is out of phase. Light can couple to this vibration, leading to a phonon polarition. (c) Surface plasmon/phonon polaritons. Surface plasmon polaritons waves confined at the interface of a metal and vacuum due to free electrons in metals coupling with photons. Surface phonon polaritons are due to phonons coupling with photons at the interface of a polar dielectric (eg: silicon carbide) and air.

1.1.2 Phonon-Polaritons

Another class of polaritons important for metamaterials are phonon-polaritons. They are collective oscillations of optically active phonons and light which occur in polar dielectrics such as silicon carbide (SiC). They occur close to the longitudinal optical (ω_{LO}) and transverse optical phonon (ω_{TO}) frequency of these materials which are in the mid-infrared spectral range.

1.1.3 Hyperbolic Metamaterial and Effective Medium Theory (EMT)

The fundamental property of hyperbolic metamaterial is that it has metallic-like properties in one direction but has dielectric-like properties in an orthogonal direction. Hyperbolic metamaterial is usually considered as a uniaxial crystal ($\varepsilon_{xx} =$

$\varepsilon_{yy} \neq \varepsilon_{zz}$)

$$\begin{bmatrix} \varepsilon_{xx} & 0 & 0 \\ 0 & \varepsilon_{yy} & 0 \\ 0 & 0 & \varepsilon_{zz} \end{bmatrix} \tag{1.1}$$

with extreme anisotropy $\varepsilon_{xx}\varepsilon_{zz} < 0$.

The dispersion relation for TE (transverse electric) and TM (transverse magnetic) waves in materials are then given by:

$$TE : \frac{{k_x}^2 + {k_y}^2}{\varepsilon_{xx}} + \frac{{k_z}^2}{\varepsilon_{xx}} = \left(\frac{\omega}{c}\right)^2 \tag{1.2}$$

$$TM : \frac{{k_x}^2 + {k_y}^2}{\varepsilon_{zz}} + \frac{{k_z}^2}{\varepsilon_{xx}} = \left(\frac{\omega}{c}\right)^2 \tag{1.3}$$

The isofrequency surface for an isotropic dielectric ($\varepsilon_{xx} = \varepsilon_{yy} = \varepsilon_{zz}$) is simply a sphere (Fig 1.3(a)). The phrase 'hyperbolic metamaterial' arises from the unique isofrequency surface of TM waves in such a medium (Fig 1.3 (b)(c)). Two possibilities exist depending on which direction is metallic, leading to either a single-sheeted hyperboloid or a double-sheeted hyperboloid. We classify these two systems based on the number of negative components of the dielectric tensor as type I ($\varepsilon_{xx}, \varepsilon_{yy} > 0, \varepsilon_{zz} < 0$) HMM and type II ($\varepsilon_{xx}, \varepsilon_{yy} < 0, \varepsilon_{zz} > 0$) HMM. Evidently from the isofrequency surface we can observe the existence of high-k states which have wavevectors far exceeding the free space wavevector ($k_0 = \frac{\omega}{c}$). These states are allowed to propagate within an HMM while they decay exponentially in dielectrics.

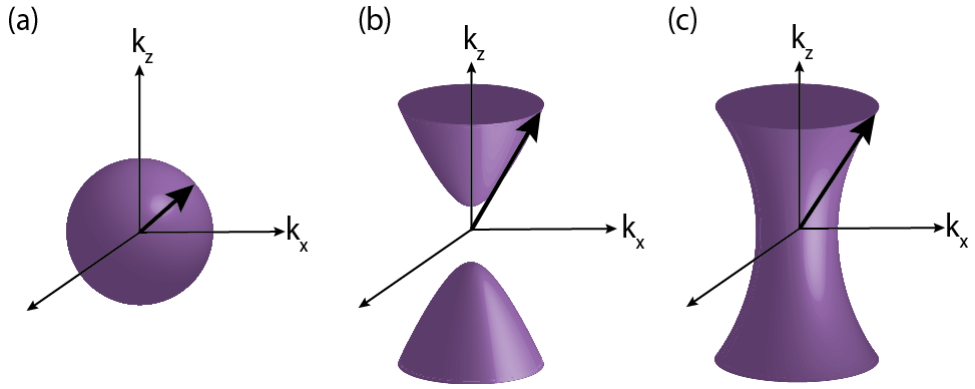

Figure 1.2: k-space isofrequency surface for (a) an isotropic dielectric, and for TM waves in (b)a type I HMM and (c) a type II HMM. The isofrequency surface is simply a sphere for waves in an isotropic dielectric. However, for TM waves in a HMM with extreme anisotropy, the isofrequency surface is either (b) a single-sheeted hyperboloid ($\varepsilon_{xx}, \varepsilon_{yy} > 0, \varepsilon_{zz} < 0$) or (c) a double-sheeted hyperboloid ($\varepsilon_{xx}, \varepsilon_{yy} < 0, \varepsilon_{zz} > 0$). The metamaterials in (b) and (c) can support unbounded wavevectors comparing to bounded wavevectors in an isotropic dielectric.

1.2 Nanowire metamaterials

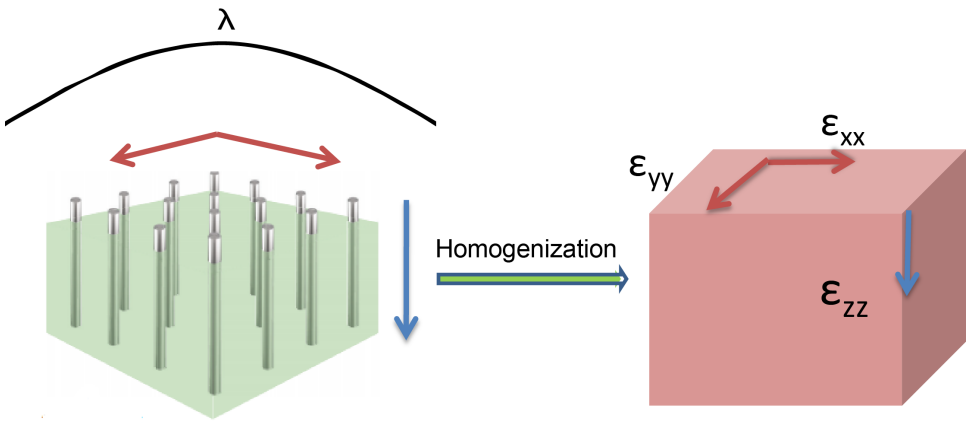

Figure 1.3: Schematics of a nanowire array. The left hand figure shows a metallic nanowire array embedded in a dielectric matrix. When the wire radius r is much smaller than the length of the wire l and both of them are much smaller than the wavelength considered, the nanowire array is approximately isotropic in the plane perpendicular to the wire axis. Therefore it can be homogenized to a uniaxial bulk medium, which has an effective permittivity along the wire axis ε_{zz} and perpendicular to wire axis ε_{xx},ε_{yy}.

This thesis focusses on a polaritonic crystal consisting of periodic metallic nanowires arranged in a host dielectric matrix. This class of nanowire metamaterials has become one of the most important artificial photonic media due to its broad bandwidth of operation, low losses and ease of fabrication. The metamaterial achieves an effective uniaxial dielectric tensor (refractive indices which are different along the wire and perpendicular to it). This is evident from the figure where we have shown that when the wavelength of radiation is much larger than the unit cell size, the medium behaves like a homogenous material with effective parameters

$$\varepsilon_{xx} = \varepsilon_{yy} = \frac{(1+f)\cdot\varepsilon_m\cdot\varepsilon_d + (1-f)\cdot{\varepsilon_d}^2}{(1-f)\cdot\varepsilon_m + (1+f)\cdot\varepsilon_d} \tag{1.4}$$

$$\varepsilon_{zz} = f\cdot\varepsilon_m + (1-f)\cdot\varepsilon_d \tag{1.5}$$

where f is fillfraction of metal The dielectric permittivity components are related to the respective refractive indices by $n_{ii} = \sqrt{\epsilon_{ii}}$ where $ii = xx, yy$ or zz.

1.2.1 Fabrication and Characterization

The nanoporous host medium for the metamaterial can either buying off the shelf anodic alumina membrane [9] or fabricated by anodizing aluminum to grow the required template [6, 10]. Multiple groups have successfully fabricated nanowire

metamaterials using both of these approaches. This template forms the basic dielectric host medium with a periodic nanoporous structure into which the silver (or gold) nanowires can be electrodeposited. Typical dimensions for recent gold nanowire structures include 20-700 nm long wires with a 10-50 nm rod diameter with 40-70 nm rod separation [6]. Note the porosity controls the fill fraction of the metal and hence the photonic modes. A multi-step controlled electrodeposition is necessary to ensure that the silver filling is consistent across the sample. Furthermore, a significant issue of silver overfilling or discontinuous islands within the pore has to be addressed after fabrication and presents a challenge to successful nanowire fabrication. This thesis deals with the theoretical and computational aspects of nanowire metamaterials and we will not discuss the fabrication or characterization.

1.3 Overview

One challenge for the field is the optical absorption or losses in the nanostructures since coupling of radiation to polaritons is always accompanied by generation of heat. This thesis deals with the thermal properties of metamaterials where optical absorption is an advantage and not a detrimental issue. The layout of the thesis is as follows:

In chapter 2, we provide a detailed analysis of the electromagnetic modes of nanowire metamaterials. We show that experimental characteristics of collective polaritons can be ascertained through the extinction spectrum of nanowire arrays.

In chapter 3, we discuss applications of thin film metamaterials for selective absorption and thermal emission applications. In particular, we consider the field of thermophotovoltaics where our metamaterial structures can be used as high temperature selective thermal emitters.

In chapter 4, we calculate the contribution of phonon-polaritons to thermal conductivity of nanowire structures. This can find important applications where the thermal conductivity has to be engineered for devices eg: thermoelectrics.

Chapter 2

Collective Polaritons of Nanowire Metamaterials

Hyperbolic metamaterials have recently emerged as one of the most promising candidates for applications such as imaging[3], absorption engineering[11], quantum [12]and thermal photonics[13]. While the 1D thin film hyperbolic metamaterial (HMM) design is well understood, a number of questions regarding the 2D nanowire HMM design remain open. In this chapter we provide insight into the unique modes of the nanowire array and explain the cases when effective medium theory is valid. We contrast the properties of gold, silver and silicon carbide nanowires for applications in the visible, near-infrared and far-infrared spectral region. We show that unique non-local modes in nanowires recently observed in far-field studies [10] can play a major role in near-field phenomena both near and away from the epsilon-near-zero spectral window.

2.1 Modes of a single nanowire: Dispersion relation and field profile

Before we study the modes of wire arrays, it will be helpful to understand the modes in a single infinitely long wire. We consider an infinite long cylinder with negative permittivity ε_2 surrounded by dielectric with permittivity ε_1 . By solving Maxwell equations, we can obtain the mode equation in a nanowire[14, 15]:

$$\begin{aligned}&\frac{m^2 {k_z}^2}{r^2}\left(\frac{1}{k_{2\perp}^2}-\frac{1}{k_{1\perp}^2}\right)^2 = \\ &\left[\frac{1}{k_{2\perp}}\frac{J_m'(k_{2\perp}r)}{J_m(k_{2\perp}r)}-\frac{1}{k_{1\perp}}\frac{H_m'(k_{1\perp}r)}{H_m(k_{1\perp}r)}\right]\times\left[\frac{k_2^2}{k_{2\perp}}\frac{J_m'(k_{2\perp}r)}{J_m(k_{2\perp}r)}-\frac{k_1^2}{k_{1\perp}}\frac{H_m'(k_{1\perp}r)}{H_m(k_{1\perp}r)}\right]\end{aligned} \tag{2.1}$$

k_z is propagation constant of the propagating mode along the wire, and $k_{1\perp}$ and $k_{2\perp}$ are the wave vectors perpendicular to wire axis in outer medium and in the wire respectively. J and H are the Bessel function and the Hankel function of the second kind respectively. m is the angular quantum number. Taking a silver wire in alumina for example, the imaginary part of the permittivity of silver is very small so we treat it as lossless.

At the wavelength of $\lambda = 1000nm$ the propagation constant of the two lowest modes, $m = 0$ mode and $m = 1$ mode, behave differently when the radius is changed (Fig.2.1 (a)). The $m = 0$ mode is highly confined at a small radius and it is the fundamental plasmonic mode irrespective of the wire radius. For the $m = 1$ mode, when the radius is very small ($r \ll \lambda$), mode equation (2.1) has a singularity and there exists only one solution $k_z = k_o$. When considering a lossy wire, $m = 1$ mode cuts off at small radius. However for large radii, this mode is plasmonic with a propagating constant $k_z > k_1$. Note, all higher order modes are cut off at a small radius.

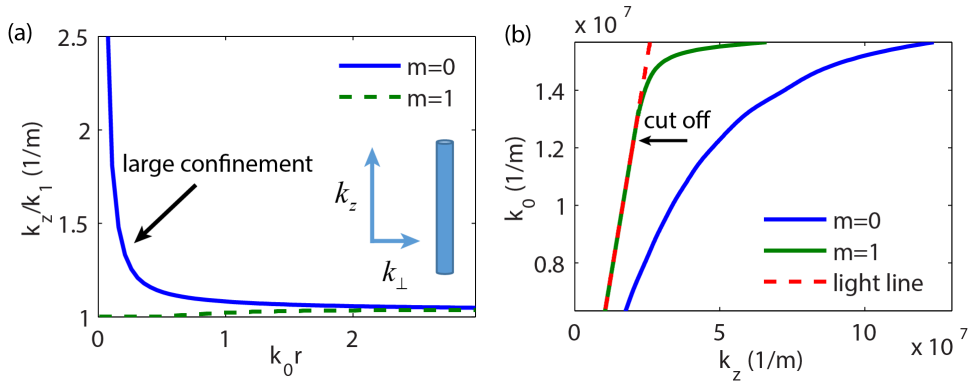

Figure 2.1: Modes of a single infinitely long silver nanowire in the low loss limit. (a) Propagation constants of the first two allowed plasmonic modes as a function of radius at the wavelength of 1000nm for a single infinite silver wire embedded in alumina ($\varepsilon = 2.74$). k_z and k_1 are the propagation constants inside and out of nanowire respectively. Blue line is $m = 0$ mode and green line is $m = 1$ mode. (b) Dispersion relation of a silver nanowire with 20nm radius. Blue line and green line are related to $m = 0$ and $m = 1$ mode respectively. Red dashed line is the light line in an alumina matrix. A single nanowire supports a fundamental $m = 0$ plasmonic mode regardless of dimensions of the wire. For a lossless metal, $m = 1$ mode (HE mode) has no cutoff revealed solving the mode equation analytically. However, in real metals, $m = 1$ mode always effectively cuts off with a small radius. Other higher modes also have corresponding cut-off radii. The arrow denotes the cutoff of $m = 1$ mode considering a real silver wire.

In order to have a more intuitive view of $m = 0$ and $m = 1$ mode, we simulated the field profile of a silver wire at the wavelength of $\lambda = 1000nm$ in Fig. 2.2. This is done by solving eigenmode equation with finite element method[16] (COMSOL

mode analysis module). It is evident that the $m = 0$ mode is a monopole mode and $m = 1$ mode is a dipole mode as expected. Furthermore, the magnetic field of $m = 0$ mode along wire axis is negligible $H_z = 0$ so that it can be classified as a TM mode. Higher modes are more complex and they are hybrid modes with both transverse and longitudinal field components (HE modes).

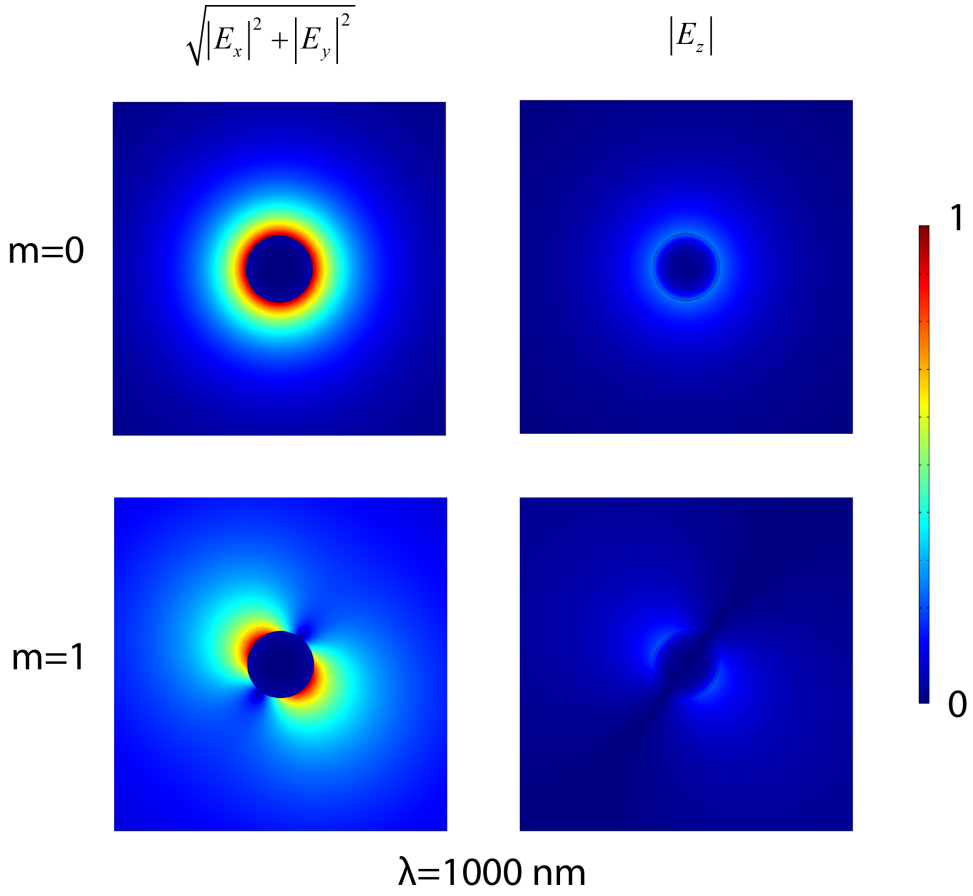

Figure 2.2: Field profile of a single wire (radius=200nm) from COMSOL at the wavelength of 1000nm. (a) and (b) are the in plane and out of plane field profiles of $m = 0$ mode. (c) and (d) are the in plane and out of plane field profiles of $m = 1$ mode. $m = 0$ mode and $m = 1$ mode are the monopole mode and dipole mode of a single nanowire respectively and both of them are plasmonic modes propagating along the wire.

2.2 Optical response of the nanowire arrays

As a 2D hyperbolic metamaterial, the nanowire array shows special optical properties[6]. In the case of gold nanowire arrays, the extinction spectra from a full-wave simulation (Fig. 2.3(a)), two resonances are found in the optical region. One is a transverse (T) resonance originating from the coupling between electromagnetic waves and the

transverse free electron oscillations. The other one is a longitudinal (L) resonance originating from the coupling between electromagnetic waves and the longitudinal electron oscillations. The direction transverse is defined as perpendicular to the cylindrical nanowire's long axis.

T resonance does not change with polarization while L resonance only occurs with p-polarized light when effective permittivity along the wire ε_{zz} is near 0. When the incident angle is 40 degrees, the averaged field magnitude is enhanced by about 5 times at T resonance and by about 3 times at the L resonances compared to the field at 1000nm. Consequently, we can see the enhanced absorption near these two resonances.

Effective medium metamaterial theory can also model these two resonances and shows reasonable agreement (Fig. 2.3(b)). However, there is critical difference near the L resonance. From the extinction spectra of p-polarized light incidents at different angles (Fig.2.3(a)), we see that the wavelength of L resonance changes at different angles. This indicates that the L resonance is wave vector dependent. In the effective medium picture this is explained by non-locality or spatial dispersion where the dielectric permittivity becomes wavevector dependent near the L resonance (epsilon-near-zero region). This nonlocal effect in nanowire array had been found in experiments from Zayats's group[10]. Conventional local effective medium theory is unable to describe the optical response near L resonance accurately (Fig2.3 (b)).

We also study silver nanowires embedded in alumina respectively which is another approach to achieving a nanowire hyperbolic metamaterial. Silver has similar optical properties with gold but it is much less lossy. The simulated results show no significant L resonance which is in complete contrast to the case of gold. The reason is that silver is hardly lossy in ENZ wavelength range so the absorption is very small. Besides, EMT does not work perfectly near the L resonance.

We now turn our attention to phonon-polaritonic nanowire arrays. We simulate the optical response of SiC nanowires embedded in $SiO2$ and (Fig.2.4). The SiC nanowires structure is an infrared HMM which is promising for infrared sensing[17] and thermal applications[18]. In SiC nanowires, two resonances are found in the infrared range when the effective response shows an epsilon-near- pole and epsilon-near-zero effect respectively. This is similar to the T and L resonances in a gold nanowire array. We see excellent agreement between the effective medium theory and computational calculations.

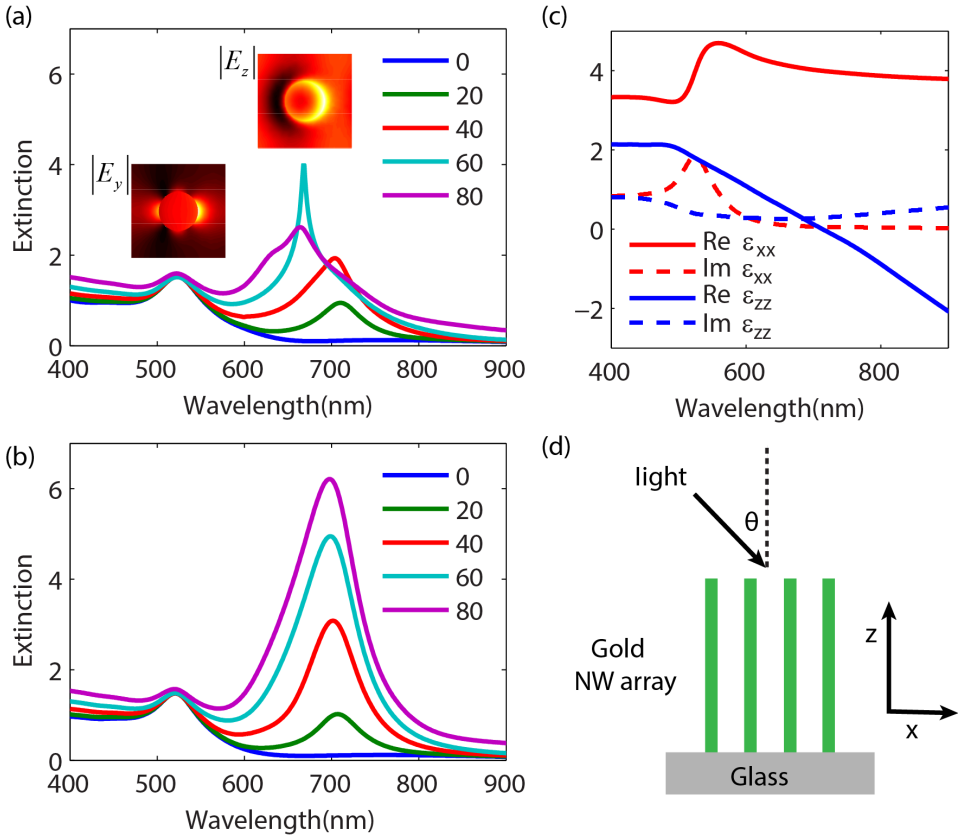

Figure 2.3: Simulated extinction spectra of gold nanowire array embedded in alumina matrix. The wire radius is 12.5nm, period is 60nm and length is 300nm. (a) and (b) are the simulated p-polarized extinction spectra at different incident angles from CST and EMT respectively. There exist longitudinal(L) and transverse(T) resonances at the wavelengths 520nm and 667nm respectively. Insets in (a) are the field profiles at the T and L resonances respectively. The field magnitude is enhanced by about 5 times at T resonance and by about 3 times at the L resonances comparing to the field at 1000nm. EMT can predict the T resonance very well while it cannot accurately predict the behavior of L resonance. (c) Effective permittivity from EMT which captures the resonances through epsilon-near-pole (ENP) and epsilon-near-zero (ENZ) behavior. Red line and blue line represent the permittivity in parallel and perpendicular direction respectively. (d) Schematic of gold nanowire array embedded in alumina on glass substrate.

2.3 Modes of nanowire arrays: Field profile from mode analysis

In order to explore the origin of these unique optical responses in the nanowire array, we now study the associated modes in detail. We consider the gold nanowires as an example but the conclusions are valid for any polaritonic nanowire array in a dielectric host matrix. We find three fundamental modes dominating the optical properties, ie. TE mode, HE1 mode and HE2 mode. Higher order modes are

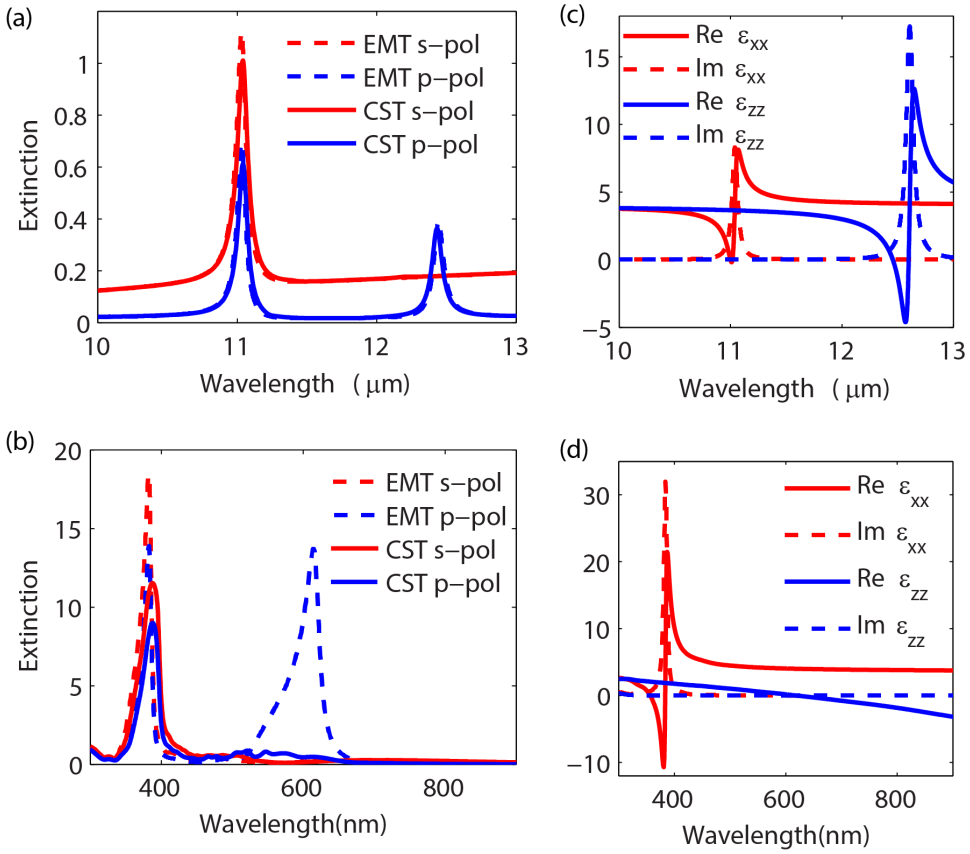

Figure 2.4: Simulated extinction spectra of (a) SiC nanowire array embedded in SiO_2 ($\varepsilon = 3.9$) and (b) silver nanowire embedded in alumina at 60 degrees incidence from CST and EMT respectively. The SiC nanowire radius is 10nm, period is 100nm and length is 1000nm. Blue solid line and red solid line represent CST's result in s-polarized and p-polarized cases respectively while blue dashed line and red dashed line represent EMT results in s-polarized and p-polarized cases respectively. (c) and (d) are the EMT permittivity of SiC nanowire and silver nanowire respectively. Blue line and red line represent the permittivity in parallel and perpendicular direction respectively. The SiC nanowire shows two main resonances at ENZ and ENP wavelengths respectively. Silver nanowires behave similar to gold nanowire but its' L resonance is not significant because silver has low loss around 600nm.

extremely dissipative modes and they do not couple to plane waves efficiently so we ignore their effects on propagating wave solutions inside nanowires.

2.3.1 TE mode

The field profiles of the TE mode (Fig 2.5) is very similar to TE polarized light scattered by a metallic cylinder. It is a dipole mode which originates from interaction between transverse component of electric field and free electrons of nanowire array (field perpendicular to long axis of the nanorod). The electric field along the wire

axes $|E_z|$ of TE modes is basically zero so it can only couple to transverse electromagnetic field. The good agreement of dispersion relation between the TE mode calculated from theory and s-polarized wave in nanowires obtained from simulations (Fig 2.8(a)) confirms our judgment.

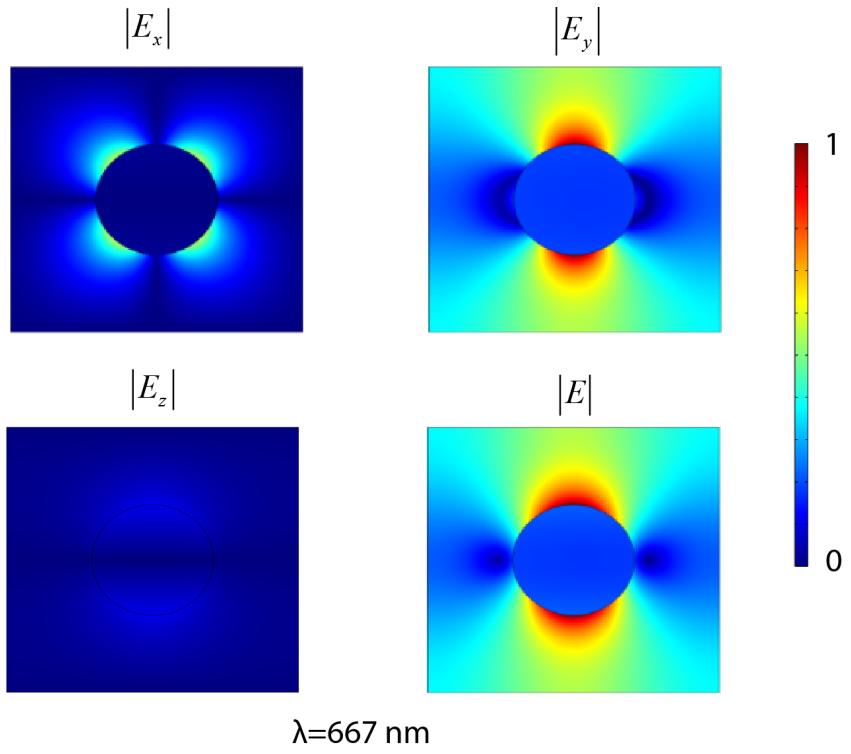

Figure 2.5: Field profile of TE mode of gold nanowire arrays from COMSOL mode analysis at the wavelength of 667nm (L resonance) and the incidence angle of 60 degrees. Wire radius is 12.5nm and period is 60nm. TE mode is a dipole mode which originates from interaction between transverse component of electric field and free electrons in gold wire.

2.3.2 HE1 mode

For HE1 mode, the non-zero field along the wire $|E_z|$ is apparent from field profile (Fig 2.6(a)). We find that at larger wavelengths, HE1 mode is highly localized in the gap between neighbouring nanowires. This behavior is similar to light scattering by conducting metals[19]. In order to find the physical origin of this HE1 mode, we plotted the electric field profiles of nanowires consisting of perfect conducing conductor (PEC) in Fig 2.6(c) by setting the boundary conditions of nanowires to be PEC boundary condition. The PEC boundary condition implies that there are no parallel electric field components on the boundaries. The PEC mode field pattern is surprisingly similar to the HE1 mode and the propagation constant agrees as well.

At large wavelengths, the permittivity of gold wire varies greatly from alumina

matrix. The large impedance mismatch makes it difficult for light penetrate into the gold wire so the light is strongly scattered. Therefore the gold wires behave like perfect conducting wires and HE1 mode is very similar to the PEC mode. At smaller wavelengths the impedance mismatch is weaker so the HE1 mode represents light partly scattered by wires. We therefore conclude that HE1 mode comes from the light scattering between the wires and it is a leaky mode.

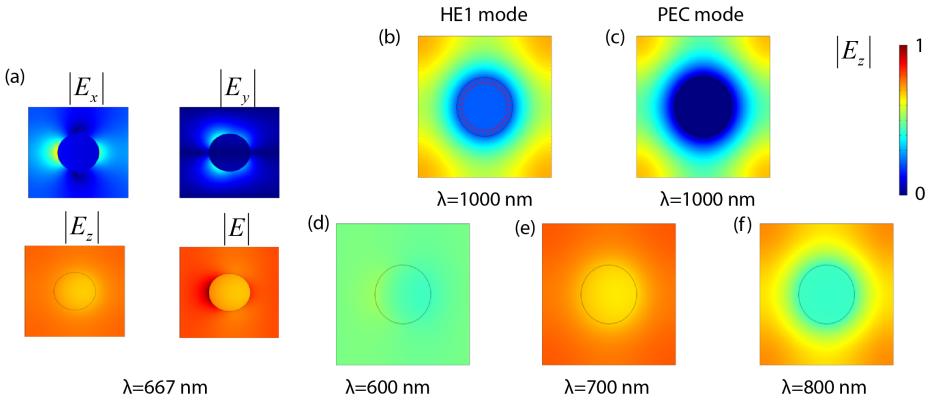

Figure 2.6: (a) Electric field profiles of HE1 mode in different directions at 667nm wavelength. E_z is the dominant component of electric field. (b)-(c) Mode profiles in z direction of (b) gold nanowire arrays (HE1 mode) and (c) perfect conducting wire arrays (PEC mode) from COMSOL mode analysis at 1000nm. (d)-(f) Mode profiles of HE1 modes at different wavelength. Wire radius is 12.5nm and period is 60nm. The larger the wavelength is, the mode is more confined and less affected by nearby wires. The HE1 mode tends to match PEC mode as wavelength increases; For example, at 1000nm the effective mode index of HE1 mode and PEC mode are 0.3103-7.2727i and -9.1725i respectively. Note that in (b) the direction and lengths of the arrows denote the in plane electric field ($\vec{E}_\perp$) direction and magnitude around the wire respectively. All the arrows are almost perpendicular to wire boundary which is close to perfect electric conditions (PEC) like in the case of a perfect conducting wire. As PEC mode is a mode arising from light scattering among conducting wires, we can interpret HE1 mode as a leaky mode among the gold wires.

2.3.3 HE2 mode

As for the HE2 mode, $|E_z|$ is dominant and the electric field is highly confined around the wire boundary. This is in stark contrast to the HE1 mode. We therefore conjecture that the HE2 mode comes from the coupling of $m = 0$ mode of each nanowire. When the wavelength is smaller HE2 mode is highly confined (Fig 2.7(d)-(f)), showing similar features as the $m = 0$ mode. By comparing the field pattern (Fig 2.7) and propagation constant of HE2 mode and $m = 0$ mode of a single wire, we confirm the description of the HE2 mode as a collective $m = 0$ mode.

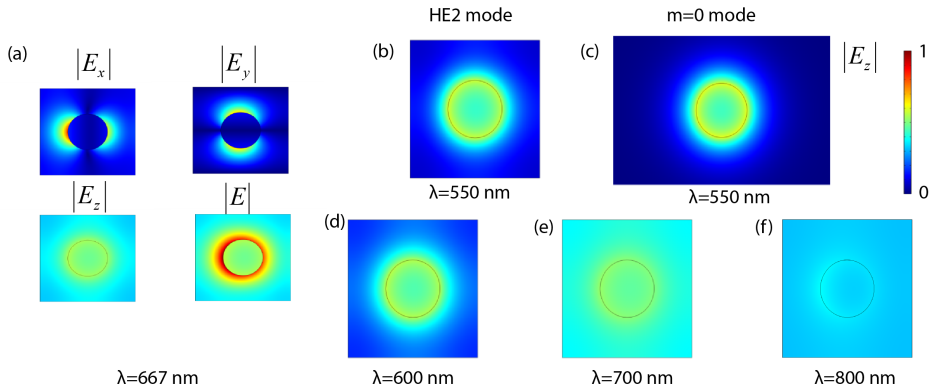

Figure 2.7: (a) Electric field of HE2 mode in different directions at 667nm wavelength. (b)-(c)Mode profiles in z direction of HE2 mode of (b) nanowire arrays and (c) a single nanowire from COMSOL mode analysis at 550nm. Wire radius is 12.5nm and period is 60nm. (d)-(f) Mode profiles of HE2 mode at different wavelengths. At low wavelengths the HE2 mode is highly confined and less affected by nearby wires. At low wavelengths it becomes a monopole mode and matches the $m = 0$ mode of a single nanowire; For example, at 550nm, the effective mode index of HE2 mode and $m = 0$ mode are 8.3171-4.1054i and 8.4594-3.7830i respectively. So we can interpret HE2 mode as a collective $m = 0$ mode.

2.4 Modes of nanowire arrays: Dispersion relation

To confirm the above analysis, we calculate the dispersion relation of each mode for gold nanowires, silver nanowires and SiC nanowires computationally and compare them to EMT dispersion relations. Gold and silver nanowires dispersion relations are similar to each other. TE mode dispersion relation matches the EMT dispersion relation of TE wave which indicates that s-polarized wave is coupled primarily to the TE mode.

For p-polarized waves, EMT always shows ENZ crossing at the L resonance. However, the results of mode analysis shows the existence of two branches corresponding to the HE1 mode and HE2 mode. It is interesting to note that the effective medium description comes from the subtle interplay of these two branches. At lower wavelengths, HE1 mode matches the EMT dispersion relation while at higher wavelengths, the EMT result is captured by the HE2 mode. In both cases, the field profile is very homogeneous.

This matching can be easily interpreted when recalling that EMT essentially homogenizes the optical properties of nanowire arrays. At wavelengths closer to the plasma frequency the HE1 mode is leaky and less confined so the field profile is more homogeneous. This is characteristic of EMT mode (black dashed line in Fig. 2.9 (b)). At large wavelengths, the HE1 mode tends to a PEC mode (still a leaky mode) and is highly confined in the matrix between nearby nanowires.

On the contrary, at small wavelengths closer to the plasmon resonance, the HE2 mode is highly confined and therefore shows strong deviations from the expected EMT model. At large wavelengths ($\lambda \gg r$),the $m = 0$ mode is less confined and approaches a homogeneous mode well-described by EMT.

It is important to note that the coupling of plane waves to nanowire metamaterials can only occur if the field variation in the metamaterial is not rapid i.e. homogenous fields are well-captured by EMT and are conducive to coupling using plane waves. EMT therfore works well at very small and very large wavelengths where only one mode with a homogenoeus profile is dominant. However, near the L resonance, both modes are partly confined so both modes couple to plane wave in the nanowire arrays, leading to a mismatch for EMT near L resonance. Because both modes are affected by k_x so this mode mixing results in a nonlocal L resonance, which is observed in Fig 2.3(a).

In the case of SiC nanowires, the situation is slightly different. TE mode dispersion is captured well by the EMT dispersion relation for s-polarized waves. However for p-polarized waves, only one mode is dominant (Fig 2.10(b)). As the wavelength is much larger than the wire dimensions, collective $m = 0$ mode is quite homogeneous and is described well by EMT. In stark contrast, the leaky mode (PEC mode) is tightly confined due to large permittivity difference between the host matrix and the nanowires. Therefore the leaky mode can be ignored and only collective $m = 0$ mode counts. Note that the extinction spectra and dispersion relations show a good agreement between theory and simulations.

2.5 Experimental Extinction Spectra

We also fabricated and characterizez gold nanowire samples with collaborations with Prof. Sandipan's group. The extinction spectra (Fig 11.(a)) shows T and L resonances at different angles. There are deviations between theory and experiment due to surface scattering effects. However, by comparing the transmittance ratio we can reduce the effects of scattering since they affect both polarizations. We note the good agreement between the transmittance ratio from experiment and simulation.

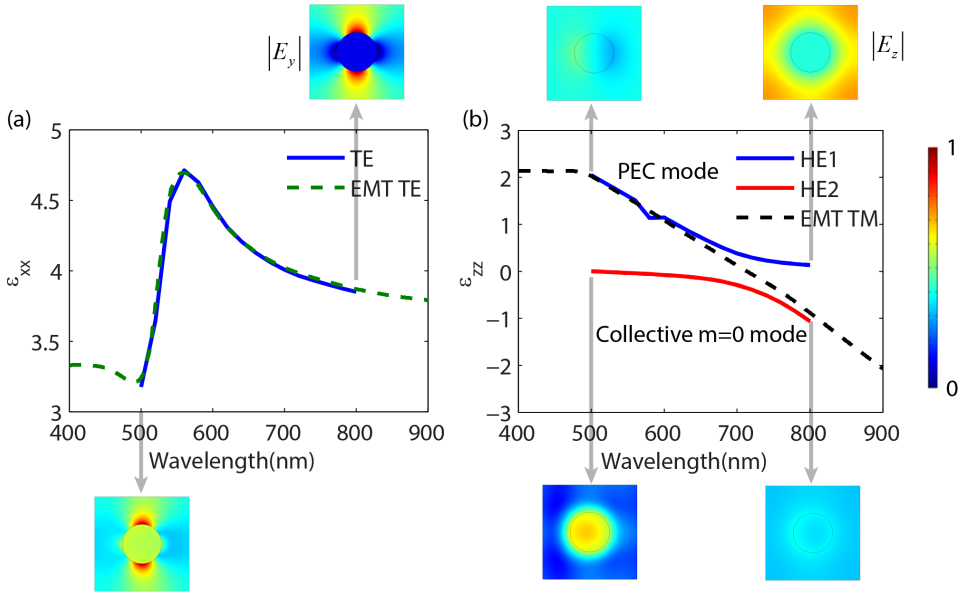

Figure 2.8: Modes dispersion relation of gold nanowire arrays from COMSOL mode analysis and EMT. Wire radius is 12.5nm and period is 60nm. Propagation constants of eigen-modes are chosen to have x axis component equal to light incident at 60 degrees. (a) Effective parallel permittivity ε_{xx} for TE mode from COMSOL mode analysis (solid line) and EMT (dashed line). The dispersion relation form TE mode analysis matches EMT results well and it implies that TE mode is the dominant mode for s-polarized waves propagating in nanowire arrays. The $|Ey|$ mode profiles at 500nm and 800nm show TE mode is a dipole mode and the large electric field component shows it is a transverse mode due to oscillation of free electrons in y direction. (b) Effective perpendicular permittivity ε_{zz} of HE1 mode (blue line) and HE2 mode (green line) from COMSOL mode analysis and EMT(red dashed line). These 2 branches indicate there exist 2 HE modes responsible for p-polarized waves. HE1 mode is a PEC-like leaky mode and HE2 mode is collective $m = 0$ mode. HE2 mode is weakly confined and the field magnitude is close to homogeneous which perfectly suits assumptions of effective medium theory. So at large wavelengths HE2 mode is the dominant mode captured by EMT. However, at small wavelengths the HE2 mode confines field around the wire while HE1 mode field profiles are more homogeneous. So at small wavelengths HE1 mode is dominant mode. Near L resonance, the electric field is enhanced and both modes are partly confined so both modes exist in the nanowire arrays, leading to a mismatch for EMT near L resonance. Because both modes are affected by k_x so this mode mixing results in a nonlocal L resonance.

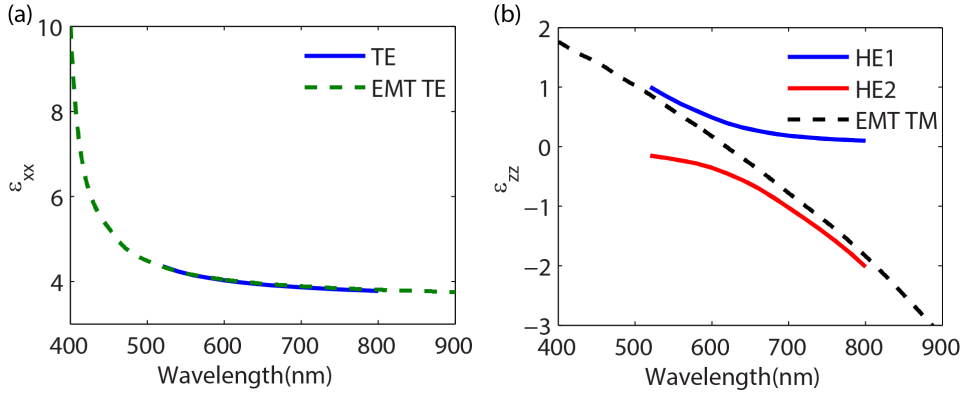

Figure 2.9: Mode dispersion relations of silver nanowire arrays from COMSOL mode analysis and EMT. Wire radius is 12.5nm and period is 60nm. (a)Effective parallel permittivity ε_{xx} for TE mode from COMSOL mode analysis(solid line) and EMT(dashed line). (b) Effective perpendicular permittivity ε_{zz} of HE1 mode (blue line) and HE2 mode (red line) from COMSOL mode analysis and EMT(black dashed line). Similar to gold nanowires TE mode is dominant for s-polarized waves while 2 HE modes are associated with p-polarized waves.

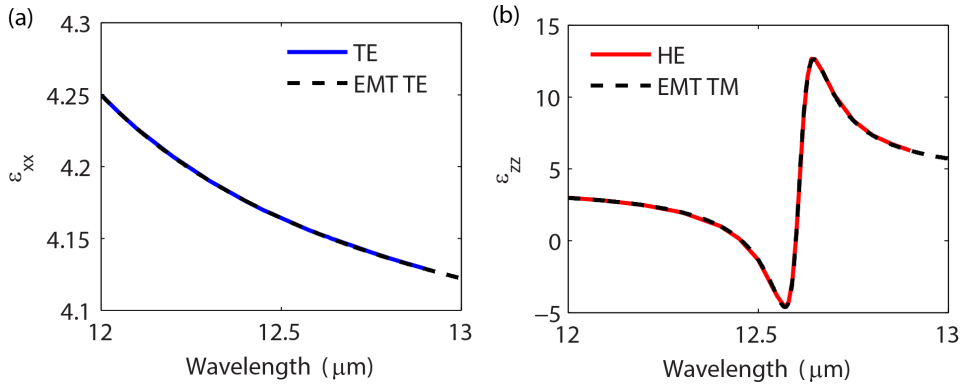

Figure 2.10: Mode dispersion relation of SiC nanowire arrays from COMSOL mode analysis and EMT. (a) Effective parallel permittivity ε_{xx} for TE mode from COMSOL mode analysis(solid line) and EMT(dashed line). (b) Effective perpendicular permittivity ε_{zz} of HE mode from COMSOL mode analysis and EMT(red dashed line). The TE mode is dominant for s-polarized waves. The HE mode is actually collective $m = 0$ mode and is the only dominant mode for p-polarized waves as the radius and period of SiC nanowire are much smaller than the wavelength considered. So we expect to see good agreement of the dispersion relation between EMT and mode analysis as well as optical responses obtained from EMT and CST simulation.

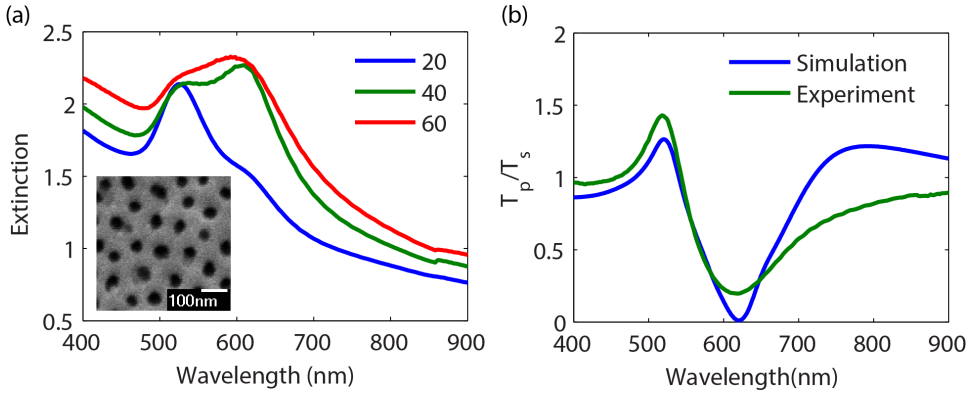

Figure 2.11: Optical response of gold nanowire from experiment. (a)The experimental extinction spectra of gold nanowire arrays at different angles. T and L resonance are easy to observe from experiment. Inset is the SEM image of fabricated gold nanowire arrays.(b) is p-polarized transmittance divided by s-polarized transmittance from experiment and CST simulation at 30 degrees incidence. In experiments the surface roughness always lead to scattering thus usually lower the transmittance. By comparing the transmittance ratio of p- and s-polarized light we can greatly reduce the scattering effect inherent in optical measurements. The good agreement between experiment and simulation confirms the metamaterial response of gold nanowire arrays.

Chapter 3

Selective Absorption and Emission

Two dimensional patterning in the form of nanoantennas[20], metasurfaces[21], gratings[22, 23] and photonic crystals[24, 25] have been used to achieve excellent selective thermal emitters for thermophotovoltaics. It was proposed by S. Molesky[11], that high temperature plasmonic thin films with tuned plasma frequency can lead to a selective thermal emitter with no patterning. This work opened a new possibility of application for plasmonics and metamaterials: high temperature nanophotonics. In this chapter, we give a detailed analysis of thin film plasmonic coatings with tuned plasma frequency. In particular, we compare selective emitters based on our proposed plasmonic coating with state-of-the-art anti-reflection coatings patented crystals[26]. We also provide intuitive insight into high temperature performance of various materials (Tungsten, Tantalum and Titanium Nitride) which can be used in thermophotovoltaics. Our results show that high temperature plasmonic coatings could potentially be a robust large area technology with transformative impact.

3.1 Blackbody radiation and emission manipulation

3.1.1 Blackbody radiation

In thermal equilibrium a blackbody can thermally radiate maximum of power to far-field. The radiation has a specific spectrum only decided by absolute temperature of the object which follows Plank's Law[27]:

$$I(\nu, T) = \frac{2h\nu^3}{c^2} \frac{1}{e^{\frac{h\nu}{kT}} - 1} \tag{3.1}$$

where $I(\nu, T)$ is the power radiated per solid angle per unit area at temperature T and frequency ν. The spectral irradiance at various temperatures are shown in Fig

3.1. The wavelength and magnitude of peak energy radiated is only determined by temperature of the blackbody.

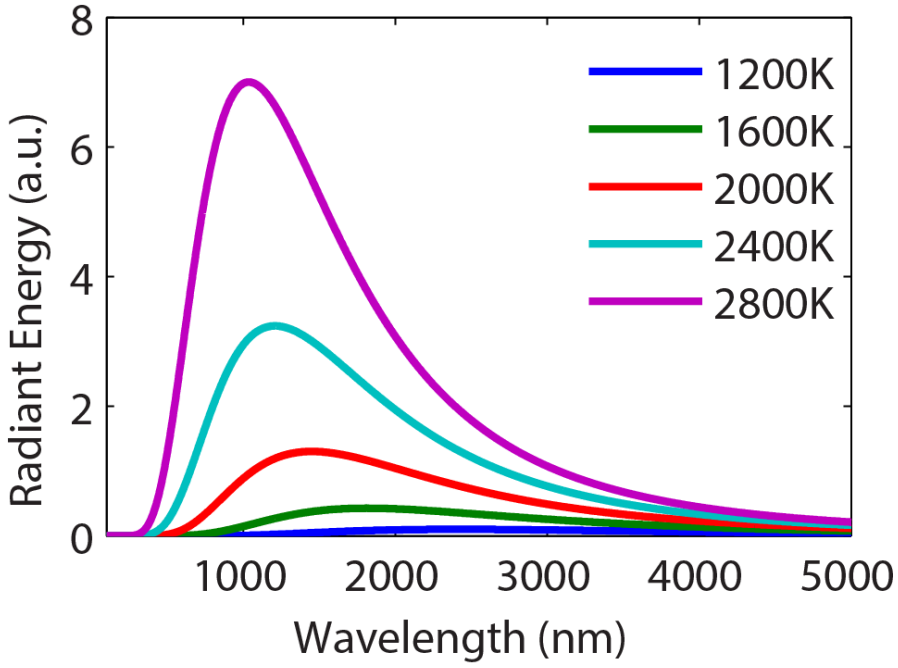

Figure 3.1: Blackbody radiation at different temperatures.

3.1.2 Kirchhoff's law of thermal radiation

Kirchhoff's law[28] of thermal radiation is a thermodynamic statement that when a body is in thermal equilibrium with its surroundings the emissivity of the body must be equal to its absorptivity at every wavelength and angle. The strength and generality of this law provides two immediate and important corollaries. First, when designing emitters that will operate in thermal equilibrium the engineering of thermal emission can be completely formulated in terms of optical absorptivity:

$$\zeta(\lambda, \theta, T) = \alpha(\lambda, \theta, T) \tag{3.2}$$

with $\alpha(\lambda, \theta, T)$ denoting the structure's absorptivity as function of wavelength, azimuthal angle, and polar angle, and $\zeta(\lambda, \theta, T)$ the structure's emissivity. Second, in the far field the thermal emission of any translationally invariant structure will be bound by the spectral radiance of a blackbody at the same temperature. The necessity of this result is clear from the definition of emissivity as direct ratio of the spectral radiance of a structure to that of blackbody at the same temperature, and the absorptivity of a translationally invariant structure being bound by unity.

From these basic principles it follows that the use of optical resonances used in all the designs we have considered provides a natural starting point for designing thin structures to control thermally excited electromagnetic radiation.

3.2 Solar TPV systems

Solar energy is one the most important energy sources in nature because of it is almost inexhaustible and clean. Conventional photovoltaic systems use semiconductors like crystalline Si to convert solar energy to electricity. However the conversion efficiency is limited by the performance of single PV cell. Solar thermophotovoltaic system is a novel energy conversion system which has an intermediate stage of converting solar energy to thermal radiation highly efficiently (Fig 3.2(c)). By using a highly absorptive absorber to heat up the emitter, photons with desired energy which match bandgap of PV cells are emitted by emitter and accepted by PV cell, leading to high thermal energy to electricity conversion efficiency. And theoretically it is possible to exceed Shockley-Queisser efficiency limit[29]. The key component in this system is the emitter design which is expected to have spectrally selective emission that can match PV cell bandgap. With plasmonic coating on conventional emitter like Tungsten and Tantalum, we can tune the emission spectrum and make ideal emitter to enhance energy conversion efficiency.

3.3 High Temperature Material Properties

The optical response of materials at high temperatures are critical to the performance of thermophotovoltaic systems. We provide here empirical models for the optical constants of refractory metals[30](tungsten, tantalum) and refractory plasmonic metals (Titanium Nitride[31]) at high temperature. We emphasize that the critical difference in these two classes of metals is the plasma frequency which when tuned to the region of thermal operation results in plasmonic behavior.

Increasing temperature causes a rise in the density of free electrons and simultaneous reduction of collision time. The effect of these dependencies is seen in a reduction of the bulk polarization response and increase in optical absorption. The two main principles to understand the change in behavior at high temperatures is the real part of the dielectric constant governing the polarization response is reduced and the imaginary part of the dielectric constant governing losses is increased. In direct connection, the performance of these components as part of a metamaterial system is reduced at high temperature. We emphasize that our designs even though extremely lossy are in fact ideally suited for selective thermal emitters since engineered losses are necessary for high emissivity according to Kirchoff's laws.

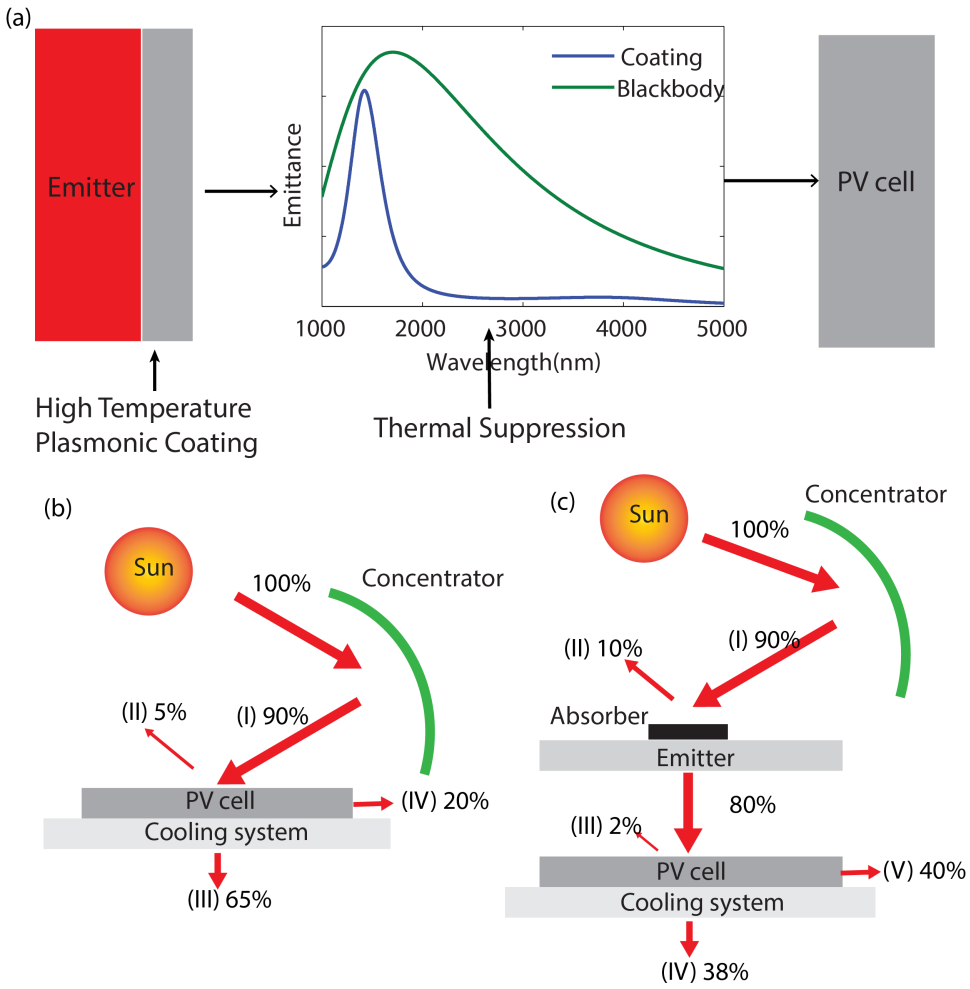

Figure 3.2: (a) With plasmonic coatings, the radiation spectrum of emitters can be directly modified to improve energy conversion performance. Photons with energy less than PV cell band gap are suppressed while photos with energy matching the PV cell band gap are enhanced. (b) Schematics of conventional solar energy conversion system. By utilizing the sunlight directly without spectral optimization the performance of PV cell is limited. Energy transfer processes consist of (i) light loss from concentrator, (ii) light loss from impedance mismatch of PV cell, (iii) energy loss as waste heat taken away by cooling system and (iv) energy transformed to electricity. (c) Schematic of solar thermophotovoltaics (STPV) system. By utilizing a near blackbody absorber to absorb solar energy and heat up the emitter to a high temperature and emit photons with desired energy, photons received by PV cell can be directly manipulated and thus achieving a higher efficiency than conventional solar PV cell system. Energy transfer processes consist of (i) light loss from concentrator, (ii) light loss from radiation of absorber, (iii) light loss from impedance mismatch of PV cell, (iv) energy loss as waste heat taken away by cooling system and (v) energy transformed to electricity.

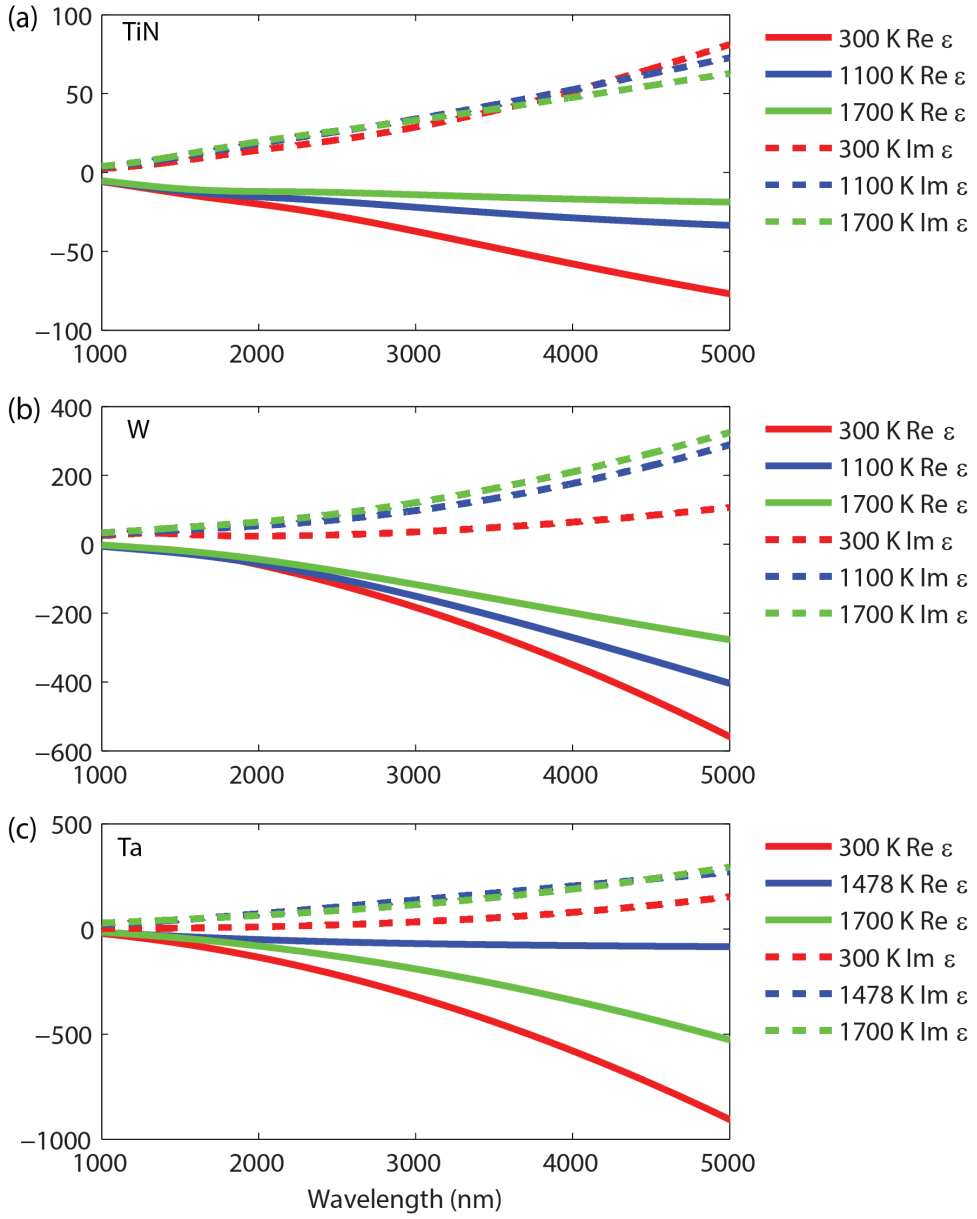

Figure 3.3: Optical properties of refractory metals at different temperatures. (a) permittivity of TiN (b) permittivity of W (c) permittivity of Ta. Data are fitted from experimental reflectance measurements.

3.4 High Temperature ENZ thin films

3.4.1 Bulk AZO

Our selective emitter relies on a simple design principle: tuning the plasma frequency of a metal with a high melting point. S. Molesky et.[11] suggested that Titanium Nitride forms an excellent choice for this application. Another option is Aluminum doped Zinc Oxide (AZO) but the dissociation effects and doping change at high

temperatures have to be carefully considered. Note that the dielectric constant approaches zero at the bulk plasma frequency. The presence of losses inevitable in metals dictates the figure of merit of all plasmonic effects including thermal emission. Sharp spectral features in emissivity will be curtailed by the presence of losses but we show how to overcome this limitation with careful design considerations.

We first start by using Kirchoff's laws to calculate the emissivity of a bulk film of AZO. Below the bulk plasma frequency (above the ENZ wavelength) large reflections curtail the absorption. This forms a simple design principle to curtail the emissivity at higher wavelength regions. We emphasize that suppressing thermal emission by this simple approach can have major implications for thermophotovoltaics since low energy (large wavelength) below bandgap photons are the primary cause of efficiency decrease. Near the bulk plasma frequency, the impedance mismatch with vacuum is reduced leading to better absorption characteristics. There is also increased absorption in these wavelength regions due to epsilon-near-zero field enhancement effects. The dispersion of the metal dictates the spectral lineshape of the emissivity. Sharp cut-offs are generally difficult with isotropic thin film ENZ media due to large absorption in the metal. Another problem is the absorption cut-off wavelength depends on the angle of incidence, which should be avoided in TPV design.

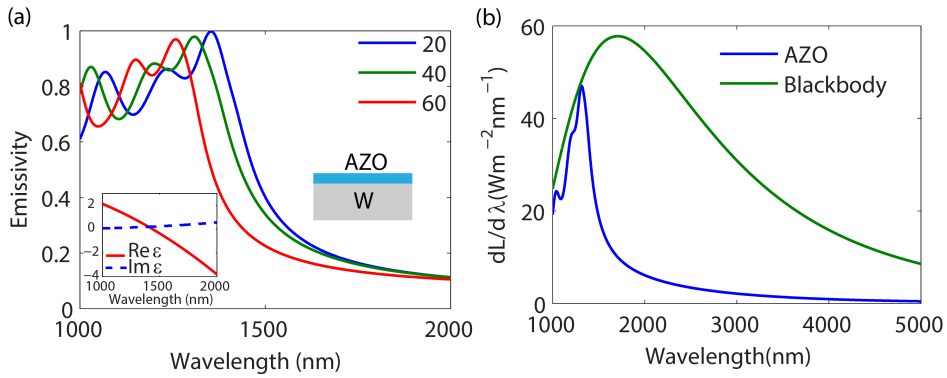

Figure 3.4: Emissivity spectra of 1000nm thick bulk AZO on W substrate at different incident angles. Inset: real part and imaginary part of permittivity of AZO. Near 1400nm due to both small impedance mismatch and electric field enhancement of ENZ resonance, the emissivity is enhanced. Beyond ENZ resonance, the emissivity is suppressed by large impedance mismatch. (b) Spectral irradiance $dL/d\lambda$ at 1700K and 40 degrees emission.

3.4.2 Multilayer(W-HfO2)

As opposed to isotropic thin films, anistotropic thin film metamaterials can achieve a better selective emitter performance. We consider a multilayer thin film structure consisting of 5 pairs of Tungsten and HfO_2 with two different fill fractions of metal.

The thickness of the layers are chosen to be far below the operating wavelength. In this case, the stack can be treated by effective medium theory. The optical response is plotted in Fig 3.5. We can see that the metamaterial has an epsilon-near-zero crossing around 1512 nm wavelength region. Below 1512nm wavelength, the multilayer structure behaves like a dielectric and experience low reflectance. Beyond 1512nm the multilayer structure becomes very reflective like a metal (Fig 3.5(a)). We note the excellent cut-off in spectral emissivity near the ENZ wavelength in perfect agreement with out design principle. The wavevector isofrequency surface changes from a ellipsoid to a hyperboloid when wavelength increases across ENZ region. The "phase transition" results in optical property change and thus a cutoff feature appears.

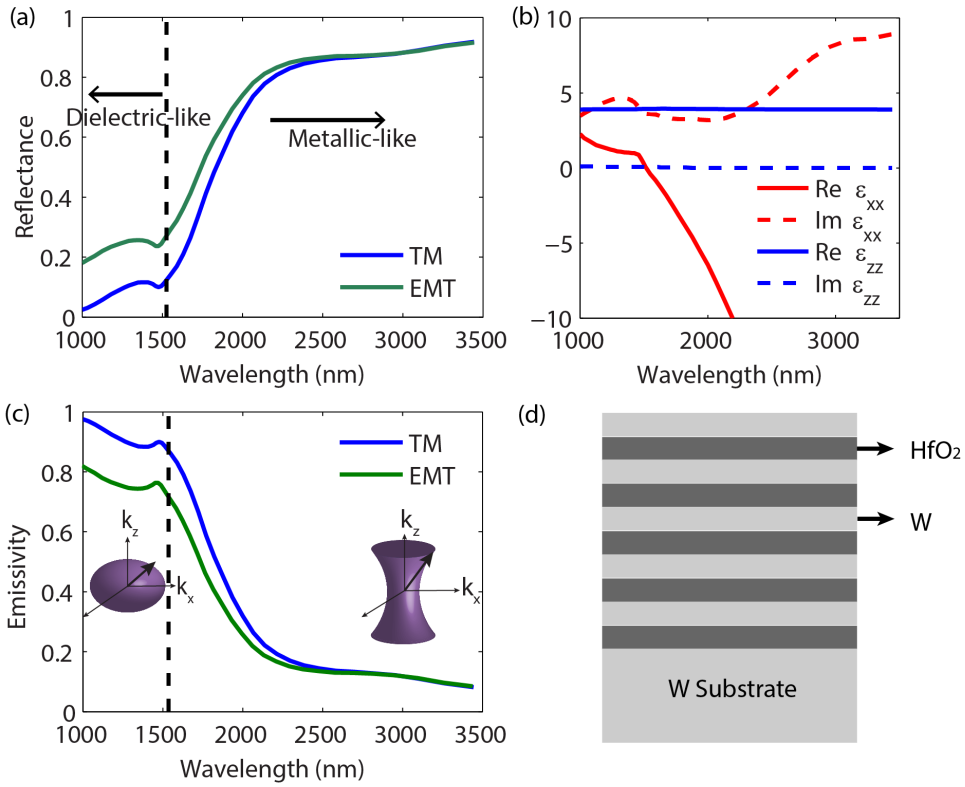

Figure 3.5: Optical properties of HfO_2/W multilayer structure. (a) Calculated reflectance by TM method (blue line) and EMT (green line). (b) Real and imaginary part of EMT permittivity. (c) Emissivity spectra. The multilayer behaves like a metal as it is very reflective at large wavelength while at smaller wavelength the reflectance resembles a dielectric's performance. This different behavior results from a drastic EMT permittivity change at 1512nm while epsilon-near-zero resonance occurs. Note that a "phase transition" occurs at ENZ resonance. When the wavelength is smaller than 1512 nm, permittivity in both direction are positive and the isofrequency surface is ellipsoid. For wavelengths larger than 1512nm, the permittivity in x-direction is negative and the isofrequency curve is hyperbolic (type II regime).

3.5 Nanowire array (TiN-AlN)

As proposed by S. Molesky et.[11], selective absorption can be achieved by tuning the epsilon-near-pole resonance of nanowire arrays to match PV cell bandgap. Embedded nanowires allow nearly free electron propagation along the perpendicular direction, but not in the parallel plane. The perpendicular direction now follows the frequency dispersion characteristics of a metal, while the parallel mimics that of an effective Lorentz model dielectric (Fig 3.6(b)). By noting that the optical properties along the wire aixs are only of importance for p-polarized light at large polar angles. The overall emissivity features of the metamaterial structures are therefore dominated by the perpendicular to wire axis direction component and often be accurately modeled as a homogeneous bulk medium. At ENP resonance, both s-polarized and p-polarized light are tuned to show selective emissivity (Fig 3.6(a)).

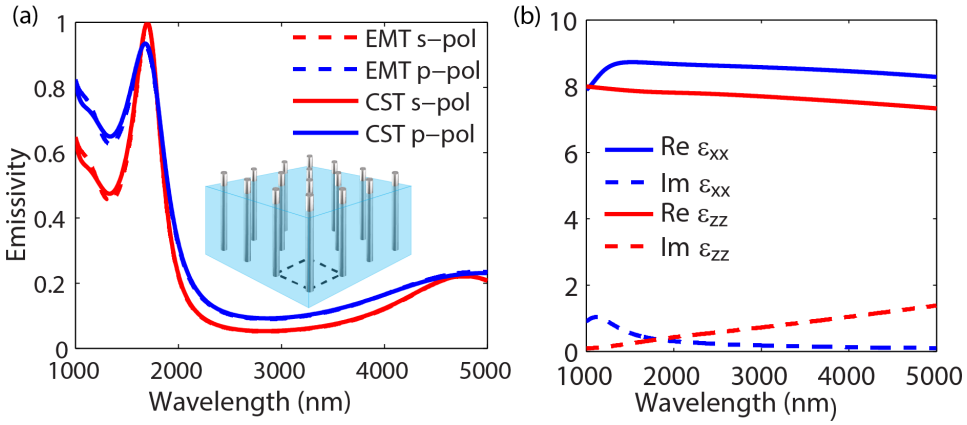

Figure 3.6: Comparison of spectral emittance of TiN-AlN nanowire calculated by CST and EMT theory. The inset of (a) shows the schematic view of TiN/AlN nanowire array on a Tantalum substrate. Nanowire radius is 15nm, period is 120 nm and thickness is 400nm. (b) Effective permittivity in the parallel and perpendicular directions respectively. The ENP resonance is centered at 1200 nm. In the ENP region, the absorption in nanowire arrays is enhanced and beyond ENP region the impedance mismatch leads to low emissivity, thus spectrally selective emission is achieved.

3.6 Photonic crystal (W PhCs)

To provide context to the Fabry-Perot ENP metamaterial design we briefly examining a photonic crystal selective emitter system. Photonic crystals present the most well developed micro-structuring approach for creating selective emitters for TPV systems, and perform this function in a variety of configurations[32]. Certain photonic crystal designs have also been experimentally verified[24]. We will consider one of the more popular of these designs, figure 2 (Fig 3.7). The principle benefit of

this scheme being that the single material system (tungsten with periodic cylindrical holes) will have greater tolerance to the thermal expansion that will occur during high temperature operation. The normal spectral emissivity of a tungsten photonic crystal, using the temperature dependent model is shown in Fig 3.3(b). The sharp cut-off in the spectral emissivity is because of the photonic bandgap effect where thermal energy density is reduced inside the medium and consequently thermal emission is suppressed. We note that this sharp cut-off in emissivity is important for thermophotovoltaics since it is precisely these large wavelength photons below the semiconductor bandgap which lower energy conversion efficiency.

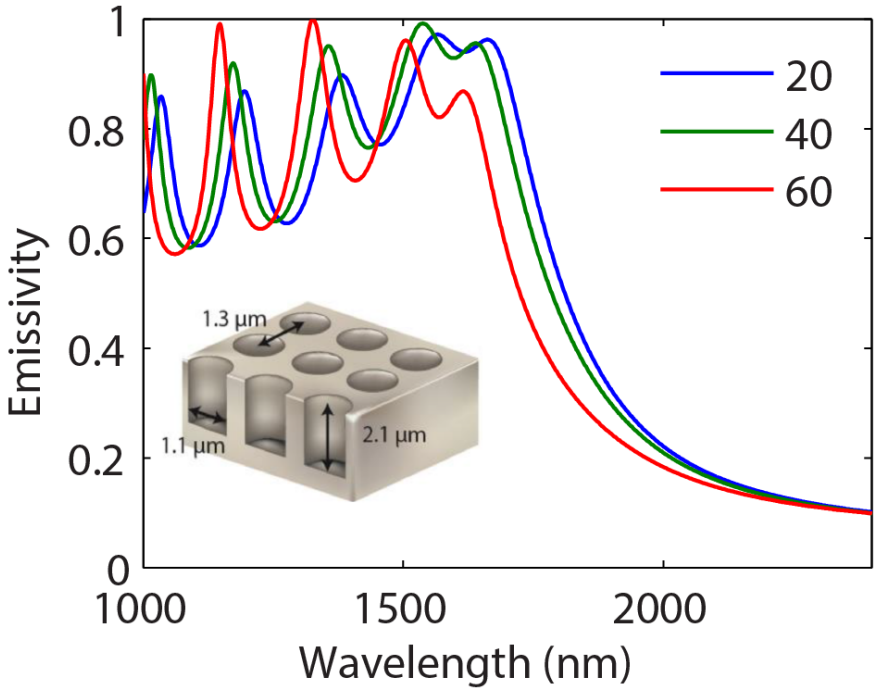

Figure 3.7: Emissivity of Tungsten photonic crystals at different angles. Inset is the PhC structure. By controlling the bandgap of photonic crystals we can make the emissivity cut-off match the PV cell bandgap.

3.7 AR coating (TiO2 on W substrate)

One simple way to achieve selective absorption is using an anti-reflection coating to modify the absorption property of substrate. Bulk tungsten has low absorption in the infrared region. By tuning the Fabry-Perot mode of a thin dielectric film, it is possible to significantly enhance the absorption selectivity of Tungsten substrate (Fig 3.8(a)). At the Fabry-Perot resonance wavelength, the thin film work as a anti-reflection coating to enhance the field in Tungsten within the skin depth, leading to

high absorption. Away from the resonance, the field inside Tungsten is not enhanced or even suppressed, leading to low absorption. The easy design and flexibility for various materials are of great potential for thin film coating to achieve selective emissivity.

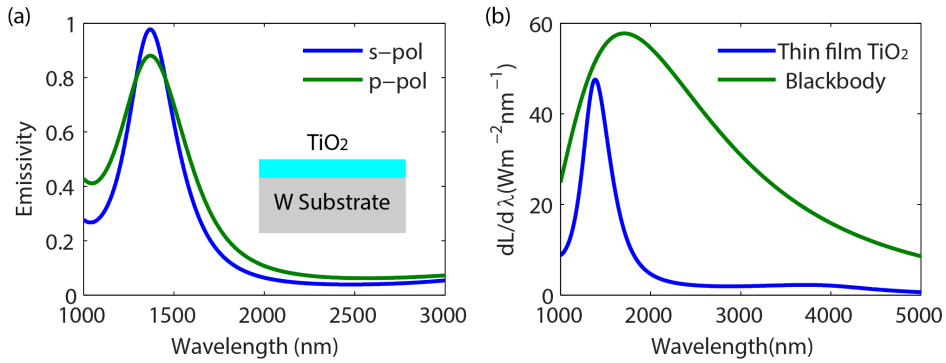

Figure 3.8: (a) Emissivity of a layer of 355nm thick TiO_2 on Tungsten substrate at 2 different polarizations at 40 degrees emission. Inset is the schematic view. (b) Spectral irradiance of a blackbody and the one layer design at 1700K. The enhanced absorption at a certain wavelength comes from the Fabry-Perot mode resonance so the peak emittance can be easily tuned by changing the thickness. The wavelength selectivity can be tuned to match PV cell to enhance energy transfer efficiency of TPV and STPV systems.

We now discuss the emissivity at high temperatures calculated using appropriately modified optical constants. The inclusion of temperature dependent optical properties has significant effect on the behaviour of the photonic crystal emitter as well as the metamaterial selective emitter. For the tungsten photonic crystal, increased emissivity is seen in the photonic bandgap with rising temperature[24] as the absorptivity of tungsten becomes larger which has a effect of reduced spectral selectivity.

The loss of spectral selectivity at high temperature causes the thermal emission of additional sub-bandgap photons. Since theses photons have very low probability of creating current, a twofold reduction in efficiency is seen. First, the photons funnel heat energy away from the emitter. More energy must then be used to maintain the emitter at constant temperature. Second, the photons are likely to be absorbed by the photovoltaic cell or TPV container. In absorbing this energy, the temperature of the photovoltaic cell and container of the TPV system will be raised, reducing electrical conversion efficiency.

Chapter 4

Polaritonic Thermal Conductivity

4.1 Thermal Conduction and Heat Carriers

Heat conduction represents the energy transfer processes through the hot side of a medium to the cooler side due to thermal motion of heat carriers in the substance. It is usually modeled by the basic Fourier Law which states the heat flux is proportional to temperature gradient:

$$\vec{J} = -k\nabla T \tag{4.1}$$

where k is the thermal conductivity. Evidently control over the thermal conductivity through nanostructuring can help in the engineering of heat transport for a multitude of applications. The thermal conductivity of some common materials are listed in Table 1.

In solids, the heat conduction can take place due to free electrons as in the case of metals or lattice vibrations (phonons) which is the dominant mechanism for insulators. There can be net photonic thermal transport inside media as well but this contribution is usually negligible unless at high temperatures [33]. Our goal in this chapter is to study how polaritons which are collective excitations of light and matter can contribute to the thermal conductivity in solids. Specifically in nanostructures, these alternative heat carriers can arise due to size confinement and they make a contribution to the thermal conductivity of the material. Thus the thermal conductivity is not only related to the intrinsic properties of material itself but also affected by the associated nanostructure. We will focus on the nanostructure thermal conductivity due to surface phonon polaritions (SPhP) and explore how it changes in different dimensions.

Substance	t,°C	K_s,W/m/K	Substance	t,°C	K_s,W/m/K
	Metal			Liquid	
Silver	0	429	Mercury	0	7.82
Copper	0	403	Water	20	0.599
Iron	0	86.5	Acetone	16	0.19
Tin	0	68.2	Ethyl	20	0.167
Nonmetallic material				Gases	
Sodium	0	6.9	Hydrogen	0	0.1655
Tourmaline	0	4.6	Helium	0	0.1411
Glass	18	0.4-1.0	Oxygen	0	0.0239
Wood	18	0.16-0.25	Nitrogen	-3	0.0237
Asbestos	18	0.12	Air	4	0.0226

Table 4.1: Thermal conductivity for various substances at atmospheric pressure and moderate temperatures[34].

4.2 Heat Carrier Transportation Process

In a system of N particles, the number of variables is usually $6N$, because of 3 space and 3 momentum coordinates. In order to reduce the number of variables people use one-particle distribution function to describe the system by averaging the N-particle distribution function. Then only 6 coordinates exist for monatomic atoms. Considering collision between particles, the one-particle distribution function $f(t, \vec{r}, \vec{p})$ follows *Boltzmann transport equation*:

$$\frac{\partial f}{\partial t} + \frac{\vec{p}}{m} \cdot \nabla f + \vec{F} \cdot \frac{\partial f}{\partial \vec{p}} = \left(\frac{\partial f}{\partial t}\right)_{collision} \tag{4.2}$$

where m is the effective mass and $\vec{F}$ is the external force acting on the particle. $\left(\frac{\partial f}{\partial t}\right)_{collision}$ measures the distribution function change due to collisions among particles.

This equation is difficult to solve generally. When considering that the state after collisions between particles are small perturbations to the equilibrium state, *relaxation time approximation* can be applied,

$$-\frac{f - f_0}{\tau} = \left(\frac{\partial f}{\partial t}\right)_{collision} \tag{4.3}$$

where τ is the total relaxation time and f_0 is the distribution function in equilibrium, such as Fermi-Dirac and Bose-einstein distributions. By neglecting inhomogeneity and external force, The BTE becomes:

$$\frac{\partial f}{\partial t} = -\frac{f - f_0}{\tau} \rightarrow f = f_0 + Ce^{-t/\tau} \tag{4.4}$$

which means once the system is slightly perturbed from equilibrium it will exponentially restore to equilibrium state. Relaxation time is a measure of the time it takes during this process. The detailed derivation of BTE and relaxation time approximation is beyond the scope of our discussion and they can be found in textbooks[35].

4.3 Net Heat Flux and Density of States (1D, 2D and 3D)

In the calculation of heat flux at a certain position $\vec{r}$, all carriers around $\vec{r}$ moving in all directions may contribute to the net heat flux in a certain direction. So we need the distribution function f in k-space which is associated with momentum as well as the density of states $g(\omega)$ which is associated with energy. In different dimensions the density of states varies. In Table 4.2 we listed the derived expressions for density of states and related thermal conductivity in 1D (nanowire), 2D (thin film) and 3D (nanowire arrays) cases. The derivation can be found in Appendix B.

Dimensions	Density of States	Thermal Conductivity
1D	$g_{1D}(\omega) = \frac{1}{\pi v_g}$	$\frac{1}{\pi r^2}\int_\omega v\hbar\omega\Lambda\frac{df_0}{dT}g_{1D}(\omega)d\omega$
2D	$g_{2D}(\omega) = \frac{k}{2\pi v_g}$	$\frac{1}{2t}\int_\omega v\hbar\omega\Lambda\frac{df_0}{dT}g_{2D}(\omega)d\omega$
3D	$g_{3D}(\omega) = \frac{k^2}{2\pi^2 v_g}$	$\frac{1}{4\pi^2}\sum_{k_z>k_0}\int_0^{\frac{\pi}{a}}\int_\omega \hbar\omega\Lambda_z\frac{df}{dT}k_x dk_x d\omega$

Table 4.2: Density of states and thermal conductivity in different dimensions.

The surface phonon polariton follows the Bose-Einstein distribution:

$$f_0 = \frac{1}{\exp(\hbar\omega/k_B T) - 1} \tag{4.5}$$

where k_B is the Boltzmann constants and T is temperature in Kelvin.

4.3.1 Single nanowire Case

We consider the case of SiC where the heat carrier will be surface phonon polaritons. The information of carriers is embedded in the optical constants. As we discussed in

Chapter 2, higher modes in a single nanowire will be cut off for small wire radius in nano-structured materials so we only need to consider the lowest 2 modes, ie. $m = 0$ mode and $m = 1$ mode. These two phonon-polaritonic modes which arise due to coupling of optically active phonons to light will contribute to the thermal conductivity.

We consider an infinitely long SiC wire embedded in vacuum with radius of 300nm. The calculated thermal conductivity along the wire is 0.0007 W/m/K. Interestingly in one dimension, the density of states and group velocity completely cancel in the 1D case. The thermal conductivity is determined completely by the mean free path of the mode. By following the work done for superlattices[36] and electron energy bands[37], the mean free path is given by $\frac{1}{2\mathrm{Im}k}$ which is proportional to the propagation length of SPhPs. The mean free path is shown in Fig 4.1(b). The $m = 0$ mode is the only contribution to thermal conductivity because other modes are completely cutoff. There are two issues affecting the thermal conductivity at different radii. One is the $1/r^2$ term in thermal conductivity expression. Another factor is the propagation length of $m = 0$ mode which will decrease with smaller wire radius while the prorogating length of $m = 1$ mode will increase in this case. However, $m = 1$ mode cuts off at small radius so it cannot make any contribution to thermal conductivity in this limit.

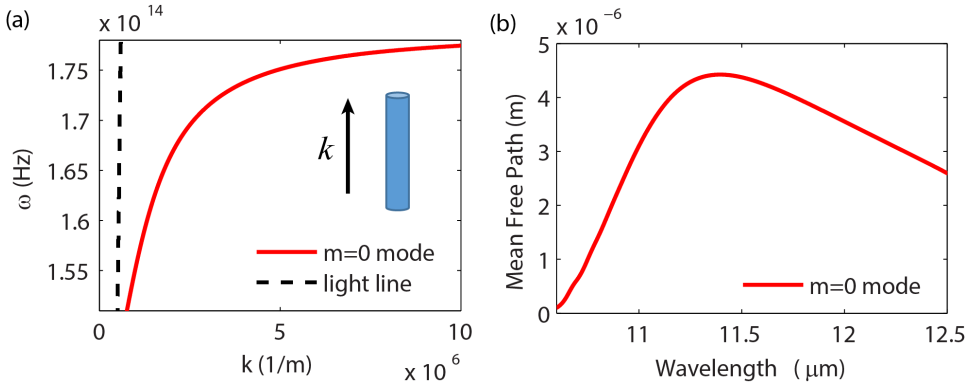

Figure 4.1: SPhP modes in a single SiC wire. (a)Dispersion relation and (b) mean free path for a single SiC nanowire. Wire radius is 300 nm. All the higher modes are not plotted because they are cutoff and have no contributions to thermal conductivity. The calculated thermal conductivity is 0.0007 W/m/K here. When radius increases, propagation length of $m = 0$ mode increases slowly. Combined with the $1/r^2$ term, the thermal conductivity is affected by changing radius. When radius keeps increasing to a certain level, $m = 1$ mode emerges and will contributes to thermal conductivity. As $m = 1$ mode is less confined we are expecting to see higher thermal conductivity contribution of $m = 1$ mode comparing to $m = 0$ mode at large radius. Note the propagation lengths are on the micron scale.

4.3.2 Thin Film Case

A thin SiO_2 slab embedded in vacuum can conduct surface phonon polariton at appropriate wavelengths the resonance frequency of optical phonons. It is well known the surface modes on thin films split into a symmetric mode and an antisymmetric mode which is given by[38]:

$$\tanh(\frac{1}{2}k_1 t) = -\frac{k_2\varepsilon_1}{k_1\varepsilon_2},\ \coth(\frac{1}{2}k_1 t) = -\frac{k_2\varepsilon_1}{k_1\varepsilon_2} \tag{4.6}$$

where t is the thickness of thin film, ε_1 and ε_2 are the permittivity of thin film and outer medium respectively. k_1 and k_2 are the propagation lengths perpendicular to thin film and outer medium respectively and can be expressed as $k_i = \sqrt{\varepsilon_i {k_0}^2 - \beta^2}, i = 1, 2$. β is the propagation constant of SPP. In Fig 4.2 we plot the dispersion relation of both modes. The thickness is chosen to be 50nm. The calculated thermal conductivity is 0.4 W/K/m which matches previous results[39]. The group velocity also cancels with density of states so that only mean free path and propagation length of SPhP counts. In Fig 4.3 we plot the mean free path with propagation constants of SPP. The mean free path of asymmetric mode is on the order of cm and is much larger than the mean free path of symmetric mode. So the asymmetric mode dominates the contribution to thermal conductivity. As these 2 modes are hardly cutoff at such small thickness, the thermal conductivity is much larger than that in single wire case. However it cannot be infinite large because the method of calculating the mean free path requires that it should be several times less than the characteristic length for heat transfer[40]. Another reason of the limitation is asymmetric mode will be cutoff at extremely small thickness[8].

4.3.3 Nanowire Metamaterial Case

In chapter 2 we have showed that for very small radius nanowire arrays, EMT can fully capture the collective polaritonic modes. So we use EMT directly to calculate the thermal conductivity.. We are considering SiC wire arrays with 100nm periodicity and 0.1 fill fraction (17.8nm radius). SiC is a phonon-polaritonic material with Reststrahlen band in the infrared spectral range between 10 μm and 12 μm. Note the TE mode originates from the transverse coupling between light and the nanowires so the s-polarized mode will not contribute to the thermal conductivity along the wire axis. On the other hand, the collective $m = 0$ mode dominates for p-polarized waves inside the SiC nanowire arrays and $m = 0$ mode is a SPhP mode travelling along the wire so it can strongly contribute to thermal conductivity.

The main contribution to SPhP mediated thermal conductivity arises in the hyperbolic dispersion regime. From Fig 4.4 we see that SiC nanowire arrays act as a type 1 hyperbolic metamaterial which supports high-k modes when the wavelength

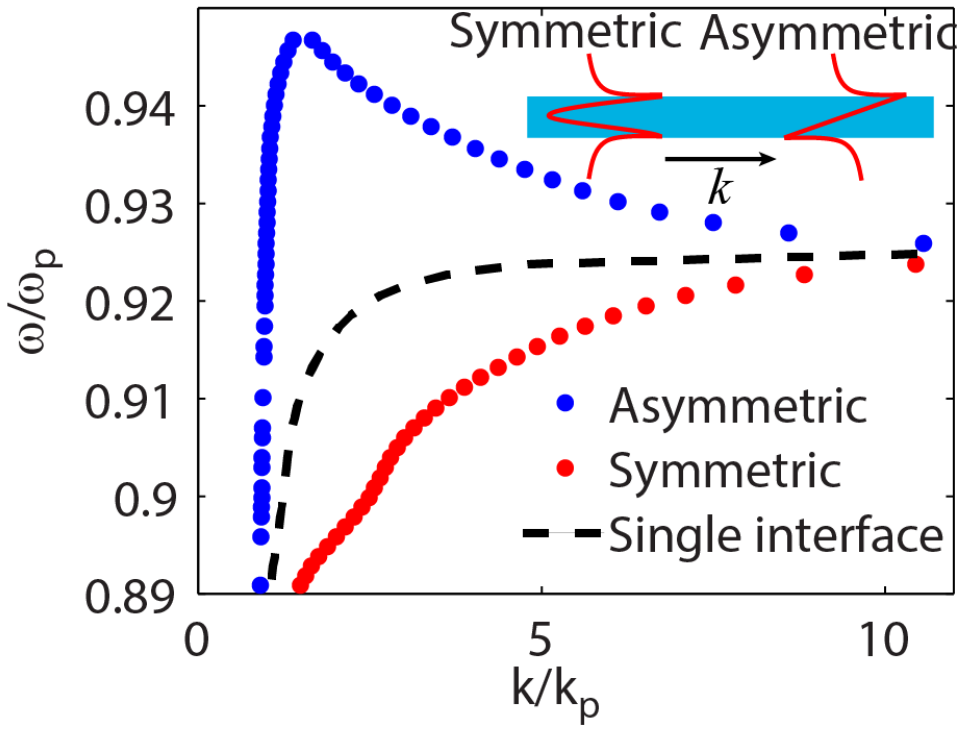

Figure 4.2: Dispersion relation of SPhP in thin film amorphous SiO_2. Asymmetric and symmetric modes come from coupling of 2 SPhP from SiO_2-air interface. The single interface SPhP dispersion is shown in black dashed line. ω_p is the longitudinal optical phonon frequency of SiO_2 which plays a role analogous to the plasma frequency of a metal since the dielectric constant passes through zero at this frequency. k_p is the related wavevector.

is larger than 11.5 μm. When the wavelength is smaller than 11.5 μm the nanowire arrays is an elliptical metamaterial which cannot support high-k modes. The calculated thermal conductivity is 0.0007 W/K/m. As has been discussed in the single wire case, when the radius is very small only the $m = 0$ mode exists and the small propagation length limits the thermal conductivity. The collective $m = 0$ mode in nanowire arrays cannot achieve a high propagation length either.

In a summary, the key factor governing SPhP mediated thermal conductivity is the propagation length of the polaritonic mode. In the case of a single nanowire as well as nanowire arrays, the fundamental limitation is the high absorption of the dominant modes. Thin film $SiO2$ can achieve a much higher level of thermal conductivity arising from the low loss asymmetric mode. It has to be mentioned that propagation length can not be infinitely large because that will break the diffusion approximation in calculating the mean free path. As the thermal conductivity of nanowire arrays is very small compared to SiC (100 W/K/m), it is reasonable to ignore the thermal conductivity due to size confinement of nanostructures when

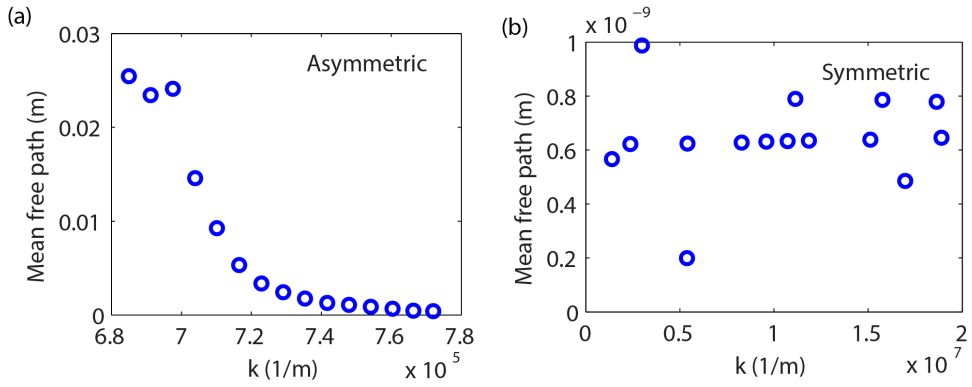

Figure 4.3: SPhP mean free path in 50 nm thin film amorphous SiO_2 for (a) asymmetric and (b) symmetric mode. Though the thermal conductivity is related to the modal propagation constants k and mean free path Λ, the mean free path of asymmetric mode can reach centimeter scales. This is much larger than the wavelength so it is still the dominant term in the thermal conductivity. We can also conclude that the thermal conductivity contribution mostly comes from the asymmetric mode. The calculated thermal conductivity is 0.4 W/K/m and is comparable with intrinsic phonon mediated thermal conductivity of SiO_2 (1 W/K/m). It has also been shown that with smaller thicknesses both propagation length and propagation constants of the asymmetric mode will increase which will lead to a thermal conductivity exceeding that of bulk SiO_2.

considering heat transfer and related thermal properties. Future work will address this issue to find ways of exploiting the phonon-polariton for nanoscale thermal conductivity engineering.

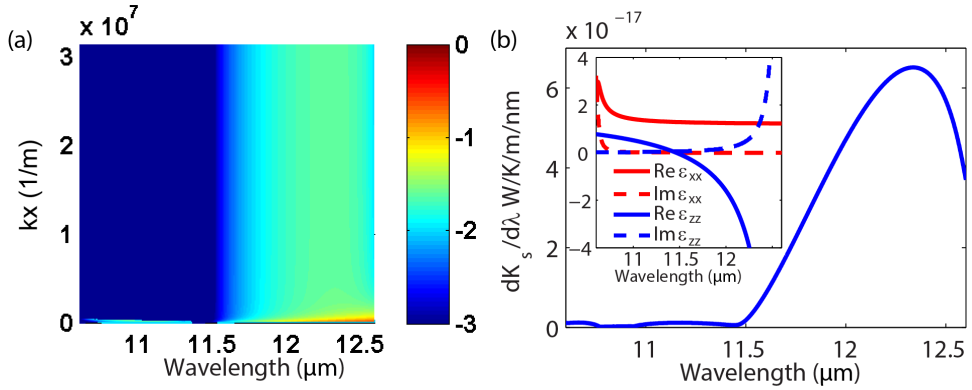

Figure 4.4: SPhP mediated thermal conductivity in SiC nanowire arrays using EMT theory. (a) SPhP mediated thermal conductivity contribution from p-polarized mode (in log scale). Note that when the wavelength is larger than 11.5 μ m thermal conductivity contribution from high wavevectors are not negligible. In this wavelength range, the nanowire arrays form a type 1 hyperbolic metamaterial, which allows high-k wave propagating inside. These high-k modes will not simply dissipated like in dielectric so they will contribute to the thermal conductivity. While beyond this wavelength range high-k mode doesn't exist and thermal conductivity contribution from this wavelength region is very small. (b) Spectral thermal conductivity. The sharp change of p-polarized mode contribution around 11.5 μm further supports that high-k mode is the main contribution for p-polarized mode. (c) Effective permittivity. The ENZ crossing occurs around 11.5 μm. The fill-fraction is 0.1 and period is 100nm.

Appendix A

EMT derivation for nanowire arrays

Following the macroscopic definition of permittivity ε,

$$\bar{D} = \bar{\varepsilon} \cdot \bar{E} \tag{A.1}$$

$\bar{D}$ and $\bar{E}$ are averaged electric displacement field and electric field. EMT relation can be derived by dividing $barD$ by $barE$. When the dimensions of nanowires are much smaller than the wavelength considered, $\bar{E}$ can be evaluated in electrostatic case.

Along the wire axis, the averaged electric field equals to each other.

$$E_m = E_d = \bar{E} \tag{A.2}$$

The averaged electric displacement field is

$$\bar{D} = \rho \cdot D_m + (1-\rho) \cdot D_d = \rho \cdot \varepsilon_m \cdot E_m + (1-\rho) \cdot \varepsilon_d \cdot E_d \tag{A.3}$$

where ρ is the fillfraction, ε_m and ε_d are the permittivity of wire and matrix respectively.

So the effective permittivity along wire axis is

$$\varepsilon_\perp = \frac{\bar{D}}{\bar{E}} = \rho \cdot \varepsilon_m + (1-\rho) \cdot \varepsilon_d \tag{A.4}$$

As for permittivity perpendicular to wire axis, the electric displacement field are the same and the averaged electric field is

$$E_m{}' = \frac{2\varepsilon_d}{\varepsilon_m + \varepsilon_d} \cdot E_d{}' \tag{A.5}$$

So the effective permittivity perpendicular to wire axis is

$$\varepsilon_{\parallel} = \frac{\rho \cdot \varepsilon_m \cdot {E_m}' + (1-\rho) \cdot \varepsilon_d \cdot {E_d}'}{\rho \cdot {E_m}' + (1-\rho) \cdot {E_d}'} = \frac{(1+\rho) \cdot \varepsilon_m \cdot \varepsilon_d + (1-\rho) \cdot {\varepsilon_d}^2}{(1-\rho) \cdot \varepsilon_m + (1+\rho) \cdot \varepsilon_d} \tag{A.6}$$

Appendix B

Thermal conductivity derivation

B.1 1D case

With relaxation time approximation,the distribution function can be written as

$$f = f_0 - \Lambda cos\theta \frac{df_0}{dx} \tag{B.1}$$

where f_0 is the equilibrium Bose-Einstein distribution function.
In the calculation of heat flux at a certain position $\vec{r}$, all carriers around $\vec{r}$ moving in all directions may contribute to the net heat flux in x direction.

$$\begin{aligned} J_{1D,x} &= \sum_{carrier} \tfrac{1}{V} \sum_{k_x} \sum_{k_y} \sum_{k_z} v_x \hbar\omega f \\ &= \sum_{carrier} \tfrac{1}{V} \int_{-\infty}^{\infty} v_x \hbar\omega f dk_x/(2\pi/L) \\ &\approx \int_{\omega} \sum_{\theta=0,\pi} \cos\theta v \hbar\omega (f_0 - \cos\theta \Lambda \tfrac{df_0}{dx}) \tfrac{g_{1D}(\omega)}{\pi r^2} d\omega \\ &= -\int_{\omega} v\hbar\omega\Lambda \tfrac{df_0}{dx} \tfrac{1}{\pi r^2} g_{1D}(\omega) d\omega \end{aligned} \tag{B.2}$$

where $g_{1D}(\omega)$ is the 1D density of states for heat carriers and Λ is the mean free path. Considering each state occupy $2\pi/L$ in k space,

$$\begin{aligned} g_{1D}(\omega)d\omega &= \tfrac{dL_k}{(2\pi/L)} \tfrac{1}{L} = \tfrac{2dk}{(2\pi/L)} \tfrac{1}{L} = \tfrac{dk}{\pi} \\ g_{1D}(\omega) &= \tfrac{dk}{\pi d\omega} = \tfrac{1}{\pi v_g} \end{aligned} \tag{B.3}$$

Recalling Fourier's Law

$$J = -K \cdot \frac{dT}{dx} \tag{B.4}$$

the thermal conductivity is

$$K_s = \frac{1}{\pi r^2} \int_{\omega} v\hbar\omega\Lambda \frac{df_0}{dT} g_{1D}(\omega) d\omega \tag{B.5}$$

B.2 2D case

Similar to 1D case, we can get the density of states and net heat flux in 2d case,

$$\begin{aligned} g_{2D}(\omega)d\omega &= \frac{dS_k}{(2\pi/L)^2}\frac{1}{S} = \frac{2\pi k dk}{(2\pi/L)^2}\frac{1}{S} = \frac{kdk}{2\pi} \\ g_{2D}(\omega) &= \frac{kdk}{2\pi d\omega} = \frac{k}{2\pi v_g} \end{aligned} \tag{B.6}$$

$$\begin{aligned} J_{2D,x} &= \sum_{carrier}\frac{1}{V}\sum_{k_x}\sum_{k_y}\sum_{k_z} v_x\hbar\omega f \\ &= \sum_{carrier}\frac{1}{V}\int_{-\infty}^{\infty}\int_{-\infty}^{\infty} v_x\hbar\omega f dk_x dk_y/(2\pi/L)^2 \\ &= \int d\theta \int_{\omega} v_x\hbar\omega f\frac{g_{2D}(\omega)}{t}d\omega \\ &= \int_0^{2\pi} d\theta \int_{\omega} v\cos\theta\hbar\omega f\frac{g_{2D}(\omega)}{t}d\omega \\ &\approx \int_0^{2\pi} d\theta \int_{\omega} v\cos\theta\hbar\omega(f_0 - \Lambda cos\theta\frac{df_0}{dx})\frac{g_{2D}(\omega)}{t}d\omega \\ &= -\frac{1}{2t}\int_{\omega} v\hbar\omega\Lambda\frac{df_0}{dx}g_{2D}(\omega)d\omega \end{aligned} \tag{B.7}$$

So the thermal conductivity is

$$K_s = \frac{1}{2t}\int_{\omega} v\hbar\omega\Lambda\frac{df_0}{dT}g_{2D}(\omega)d\omega \tag{B.8}$$

B.3 3D case

We still follow the similar procedures to derive the thermal conductivity in 3D case, eg. nanowire arrays. Nanowire arrays are actually anisotropic medium. However, because of symmetry all SPP's contribution to heat conduction will be along wire axis. So we assume that the relaxation time approximation is still valid along the wire axis and thus we get the net heat flux directly from integration in k space for SPP,

$$\begin{aligned} J_{3D,z} &= \sum_{carrier}\frac{1}{V}\int_{-\infty}^{\infty}\int_{-\infty}^{\infty}\int_{-\infty}^{\infty} v_x\hbar\omega f dk_x dk_y dk_z/(2\pi/L)^3 \\ &= \frac{1}{(2\pi)^3}\sum_{k_z>k_0}\int_0^{\frac{\pi}{a}}\int_{\omega} v_z\hbar\omega f(2\pi k_x\frac{\partial k_z}{\partial\omega})dk_x d\omega \\ &= \frac{1}{(2\pi)^2}\sum_{k_z>k_0}\int_0^{\frac{\pi}{a}}\int_{\omega} v_z\hbar\omega(f_0 - \Lambda_z\frac{df}{dz})k_x\frac{\partial k_z}{\partial\omega}dk_x d\omega \\ &= -\frac{1}{(2\pi)^2}\sum_{k_z>k_0}\int_0^{\frac{\pi}{a}}\int_{\omega} v_z\hbar\omega\Lambda_z\frac{df}{dx}k_x\frac{\partial k_z}{\partial\omega}dk_x d\omega \\ &= -\frac{1}{(2\pi)^2}\sum_{k_z>k_0}\int_0^{\frac{\pi}{a}}\int_{\omega} v_z\hbar\omega\Lambda_z\frac{df}{dx}k_x\frac{\partial k_z}{\partial\omega}dk_x d\omega, v_z = \frac{\partial\omega}{\partial k_z} \\ &= -\frac{1}{(2\pi)^2}\sum_{k_z>k_0}\int_0^{\frac{\pi}{a}}\int_{\omega}\hbar\omega\Lambda_z\frac{df}{dx}k_x dk_x d\omega \end{aligned} \tag{B.9}$$

and thermal conductivity

$$K_s = \frac{1}{4\pi^2} \sum_{s,p} \int_0^{\frac{\pi}{a}} \int_{\omega} \hbar\omega \Lambda_z \frac{df}{dT} k_x dk_x d\omega \tag{B.10}$$

Bibliography

[1] Nicholas Fang, Hyesog Lee, Cheng Sun, and Xiang Zhang. Sub–diffraction-limited optical imaging with a silver superlens. *Science*, 308(5721):534–537, 2005.

[2] Zubin Jacob, Leonid V Alekseyev, and Evgenii Narimanov. Optical hyperlens: far-field imaging beyond the diffraction limit. *Optics express*, 14(18):8247–8256, 2006.

[3] Zhaowei Liu, Stéphane Durant, Hyesog Lee, Yuri Pikus, Nicolas Fang, Yi Xiong, Cheng Sun, and Xiang Zhang. Far-field optical superlens. *Nano Letters*, 7(2):403–408, 2007.

[4] Zhaowei Liu, Hyesog Lee, Yi Xiong, Cheng Sun, and Xiang Zhang. Far-field optical hyperlens magnifying sub-diffraction-limited objects. *science*, 315(5819):1686–1686, 2007.

[5] Alexander A. Govyadinov and Viktor A. Podolskiy. Metamaterial photonic funnels for subdiffraction light compression and propagation. *Phys. Rev. B*, 73:155108, Apr 2006.

[6] AV Kabashin, P Evans, S Pastkovsky, W Hendren, GA Wurtz, R Atkinson, R Pollard, VA Podolskiy, and AV Zayats. Plasmonic nanorod metamaterials for biosensing. *Nature materials*, 8(11):867–871, 2009.

[7] John B Pendry, David Schurig, and David R Smith. Controlling electromagnetic fields. *science*, 312(5781):1780–1782, 2006.

[8] Pierre Berini. Long-range surface plasmon polaritons. *Advances in Optics and Photonics*, 1(3):484–588, 2009.

[9] MA Noginov, Yu A Barnakov, G Zhu, T Tumkur, H Li, and EE Narimanov. Bulk photonic metamaterial with hyperbolic dispersion. *Applied Physics Letters*, 94(15):151105–151105, 2009.

[10] RJ Pollard, A Murphy, WR Hendren, PR Evans, R Atkinson, GA Wurtz, AV Zayats, and Viktor A Podolskiy. Optical nonlocalities and additional waves in epsilon-near-zero metamaterials. *Physical review letters*, 102(12):127405, 2009.

[11] Sean Molesky, Christopher J Dewalt, and Zubin Jacob. High temperature epsilon-near-zero and epsilon-near-pole metamaterial emitters for thermophotovoltaics. *Optics express*, 21(101):A96–A110, 2013.

[12] CL Cortes, W Newman, S Molesky, and Z Jacob. Quantum nanophotonics using hyperbolic metamaterials. *Journal of Optics*, 14(6):063001, 2012.

[13] Yu Guo and Zubin Jacob. Thermal hyperbolic metamaterials. *Optics express*, 21(12):15014–15019, 2013.

[14] John David Jackson. *Classical electrodynamics*. Wiley, New York, NY, 3rd ed. edition, 1999.

[15] Constantine A Balanis. *Advanced engineering electromagnetics*, volume 20. Wiley New York, 1989.

[16] John D Joannopoulos, Steven G Johnson, Joshua N Winn, and Robert D Meade. *Photonic crystals: molding the flow of light*. Princeton university press, 2011.

[17] Thomas Taubner, Dmitriy Korobkin, Yaroslav Urzhumov, Gennady Shvets, and Rainer Hillenbrand. Near-field microscopy through a sic superlens. *Science*, 313(5793):1595–1595, 2006.

[18] Yu Guo, Cristian L Cortes, Sean Molesky, and Zubin Jacob. Broadband superplanckian thermal emission from hyperbolic metamaterials. *Applied Physics Letters*, 101(13):131106, 2012.

[19] Hendrik Christoffel Hulst and HC Van De Hulst. *Light scattering by small particles*. Courier Dover Publications, 1957.

[20] Paolo Biagioni, Jer-Shing Huang, and Bert Hecht. Nanoantennas for visible and infrared radiation. *Reports on Progress in Physics*, 75(2):024402, 2012.

[21] Burton Neuner III, Chihhui Wu, Gregory Ten Eyck, Michael Sinclair, Igal Brener, and Gennady Shvets. Efficient infrared thermal emitters based on low-albedo polaritonic meta-surfaces. *Applied Physics Letters*, 102(21):211111, 2013.

[22] JA Mason, DC Adams, Z Johnson, S Smith, AW Davis, and D Wasserman. Selective thermal emission from patterned steel. *Optics express*, 18(24):25192–25198, 2010.

[23] JA Mason, S Smith, and D Wasserman. Strong absorption and selective thermal emission from a midinfrared metamaterial. *Applied Physics Letters*, 98(24):241105, 2011.

[24] Yi Xiang Yeng, Michael Ghebrebrhan, Peter Bermel, Walker R Chan, John D Joannopoulos, Marin Soljačić, and Ivan Celanovic. Enabling high-temperature nanophotonics for energy applications. *Proceedings of the National Academy of Sciences*, 109(7):2280–2285, 2012.

[25] Andrej Lenert, David M Bierman, Youngsuk Nam, Walker R Chan, Ivan Celanović, Marin Soljačić, and Evelyn N Wang. A nanophotonic solar thermophotovoltaic device. *Nature nanotechnology*, 2014.

[26] Lewis M Fraas, John E Samaras, and James E Avery. Antireflection coated refractory metal matched emitters for use in thermophotovoltaic generators, August 7 2001. US Patent 6,271,461.

[27] Robert Siegel. *Thermal radiation heat transfer*, volume 1. CRC press, 2001.

[28] Jean-Jacques Greffet and Manuel Nieto-Vesperinas. Field theory for generalized bidirectional reflectivity: derivation of helmholtzs reciprocity principle and kirchhoffs law. *JOSA A*, 15(10):2735–2744, 1998.

[29] Eden Rephaeli and Shanhui Fan. Absorber and emitter for solar thermophotovoltaic systems to achieve efficiency exceeding the shockley-queisser limit. *Optics express*, 17(17):15145–15159, 2009.

[30] Yo So Touloukian. *Thermophysical Properties of Matter*. IFI/Plenum, 1976.

[31] Gururaj V Naik, Jongbum Kim, and Alexandra Boltasseva. Oxides and nitrides as alternative plasmonic materials in the optical range [invited]. *Optical Materials Express*, 1(6):1090–1099, 2011.

[32] Shawn-Yu Lin, J Moreno, and JG Fleming. Three-dimensional photonic-crystal emitter for thermal photovoltaic power generation. *Applied physics letters*, 83(2):380–382, 2003.

[33] Evgenii Narimanov and Igor Smolyaninov. Beyond stefan-boltzmann law: thermal hyper-conductivity. In *Quantum Electronics and Laser Science Conference*, pages QM2E–1. Optical Society of America, 2012.

[34] Yury V. Polezhaev. Thermal conductivity.

[35] Gang Chen. *Nanoscale energy transport and conversion: a parallel treatment of electrons, molecules, phonons, and photons*. Oxford University Press, USA, 2005.

[36] MV Simkin and GD Mahan. Minimum thermal conductivity of superlattices. *Physical Review Letters*, 84(5):927, 2000.

[37] John Brian Pendry. *Low energy electron diffraction: the theory and its application to determination of surface structure*, volume 2. Academic Press London, 1974.

[38] Stefan Alexander Maier. *Plasmonics: Fundamentals and Applications: Fundamentals and Applications*. Springer, 2007.

[39] Dye-Zone A Chen, Arvind Narayanaswamy, and Gang Chen. Surface phonon-polariton mediated thermal conductivity enhancement of amorphous thin films. *Physical Review B*, 72(15):155435, 2005.

[40] Robert Siegel and John R Howell. Thermal radiation heat transfer. *NASA STI/Recon Technical Report A*, 93:17522, 1992.